Monthly Notices of the ROYAL ASTRONOMICAL SOCIETY

MNRAS **519,** 2812–2837 (2023) https://doi.org/10.1093/mnras/stac3716
Advance Access publication 2022 December 19

Jets from SANE super-Eddington accretion discs: morphology, spectra, and their potential as targets for ngEHT

Brandon Curd,[1,2]★ Razieh Emami,[1] Richard Anantua,[1,2,3] Daniel Palumbo,[1,2] Sheperd Doeleman[1,2] and Ramesh Narayan[1,2]

[1]*Harvard-Smithsonian Center for Astrophysics, 60 Garden Street, Cambridge, MA 02138, USA*
[2]*Black Hole Initiative at Harvard University, 20 Garden Street, Cambridge, MA 02138, USA*
[3]*Department of Physics & Astronomy, The University of Texas at San Antonio, One UTSA Circle, San Antonio, TX 78249, USA*

Accepted 2022 December 13. Received 2022 December 13; in original form 2022 June 13

ABSTRACT

We present general relativistic radiation magnetohydrodynamics (GRRMHD) simulations of super-Eddington accretion flows around supermassive black holes (SMBHs), which may apply to tidal disruption events (TDEs). We perform long duration ($t \geq 81,200\,GM/c^3$) simulations that achieve mass accretion rates $\gtrsim$11 times the Eddington rate and produce thermal synchrotron spectra and images of their jets. Gas flowing beyond the funnel wall expands conically and drives a strong shock at the jet head while variable mass ejection and recollimation, along the jet axis, results in internal shocks and dissipation. Assuming the ion temperature (T_i) and electron temperature (T_e) in the plasma are identical, the radio/submillimetre spectra peak at >100 GHz and the luminosity increases with BH spin, exceeding $\sim 10^{41}$ erg s^{-1} in the brightest models. The emission is extremely sensitive to T_i/T_e as some models show an order-of-magnitude decrease in the peak frequency and up to four orders-of-magnitude decline in their radio/submillimetre luminosity as T_i/T_e approaches 20. Assuming a maximum VLBI baseline distance of 10 Gλ, 230 GHz images of $T_i/T_e = 1$ models shows that the jet head may be bright enough for its motion to be captured with the EHT (ngEHT) at $D \lesssim 110$ (180) Mpc at the 5σ significance level. Resolving emission from internal shocks requires $D \lesssim 45$ Mpc for both the EHT or ngEHT.

Key words: accretion, accretion discs – black hole physics – MHD – radiative transfer.

1 INTRODUCTION

The central black holes (BHs) of galaxies throughout the universe gain some fraction of their mass from the tidal disruption of stars in the near vicinity (see Pfister et al. 2021 for a recent study). Random scatterings of stars orbiting the BH occasionally place them on a chance orbit that will cross the tidal radius [R_t, defined later in equation (12)], beyond which the star's self gravity is weaker than the tidal forces acting on it, and it is subsequently disrupted into an elongated stream of gas (Hills 1975; Rees 1988; Evans & Kochanek 1989; Phinney 1989). The bright transient, which occurs as a result of the disruption, is known as a tidal disruption event (TDE). The most well-studied TDE is that of a near solar mass star being disrupted by a supermassive BH (SMBH). In these events, the transient light curve roughly follows a $L \propto (t/t_{fb})^{-5/3}$ decay. Here, the fallback time

$$t_{fb} = 3.5 \times 10^6\ \mathrm{s} \left(\frac{M_{BH}}{10^6\ M_\odot}\right)^{1/2} \left(\frac{M_*}{M_\odot}\right)^{-1} \left(\frac{R_*}{R_\odot}\right)^{3/2}, \quad (1)$$

where M_* is the mass of the disrupted star and R_* is its radius, is the characteristic decay time for the TDE (Stone, Sari & Loeb 2013). This behaviour originates from the gas dynamics during the disruption, which causes the star to be disrupted into an elongated stream of gas with a binding energy distribution which dictates that mass flows back towards pericentre at the 'fallback rate' $\dot{M}_{fb} \propto (t/t_{fb})^{-5/3}$ (Stone et al. 2013). The earliest theoretical works on the subject proposed that the radiation emitted by TDEs would originate from a small-scale, geometrically thick accretion disc located near $\sim R_t$ due to circularization of the stream with gas temperatures leading to X-ray/UV emission (e.g. see Rees 1988).

Thanks to various surveys in the optical/UV and X-ray, the number of known TDEs has grown substantially since their initial discovery via *ROSAT* (see Komossa 2015; Gezari 2021 for a review). We now understand that TDE emission is quite complicated as not all TDEs have bright X-ray emission. Also, the optical/UV emission follows the same power-law behaviour as expected for the X-ray. This suggests that the optical/UV component originates from reprocessed X-rays emitted from the hot accretion disc (Dai et al. 2018). The reprocessing material may be any surrounding material such as the TDE debris itself, clouds, outflows, or winds. This scenario is supported observationally as several Bowen-TDEs, which show Bowen fluorescence (requiring reprocessing of higher energy photons), have been detected (Leloudas et al. 2019; van Velzen et al. 2021).

Radio studies in the 5–8.4 GHz range have only detected emission from a handful of TDEs (Alexander et al. 2020; Pasham et al. 2022). Four of these are likely so-called 'jetted' TDEs, which launched powerful relativistic jets with bulk lorentz factor $\Gamma > 10$ and had a peak radio luminosity of $L_{peak,radio} \sim 10^{40} - 10^{42}$ erg s^{-1}. Jetted TDEs are rare, making up only a small subset ($\sim$ 1 per cent) of all TDEs (Sun, Zhang & Li 2015; Andreoni et al. 2022; Pasham et al. 2022). The other events, which emitted significantly less energy in the radio with $L_{peak,radio} \sim 10^{37} - 10^{39}$ erg s^{-1}, have been modelled

★ E-mail: brandon.curd@cfa.harvard.edu

using subrelativistic outflows, internal jet shocks, and off-axis jets. An important difference in each of these mechanisms is the site of acceleration for electrons which eventually produce the observed synchrotron emission. For example, in the external shock picture, the electrons are accelerated in the shock between the outflow and the circumnuclear medium (CNM), while in the internal acceleration picture, the electrons are accelerated inside of the jet itself.

It is worth noting that radio emission in 'non-jetted' TDEs (TDEs with no highly relativistic jet) typically appears >30 d after the discovery of the TDE in the optical/UV/X-ray bands. Assuming the outflow, which ultimately results in radio emission, is driven by the accretion flow itself, this may simply be due to the initially turbulent evolution of the disc. The infall of high-density material into the BH at steep angles may suppress the formation of a funnel region, through which the gas may be accelerated into a jet (Curd 2021). However, Bonnerot & Lu (2020) present hydrodynamical simulations of a TDE accretion disc, which appear to have formed a funnel region promptly. It is also possible that our understanding of the disc-formation process itself is incomplete. For instance, the onset of disc formation may not correlate to the time at which optical/UV/X-ray emission emerges.

TDEs are of great interest for studies of accretion physics and stellar populations close to the BH. For TDEs of Sun-like stars around BHs with mass $M_{\rm BH} \lesssim 10^{7.5}\,{\rm M}_\odot$, the peak fallback rate will exceed the Eddington rate $\dot{M}_{\rm Edd}$ (Stone et al. 2013), which opens up the possibility that the accretion rate is actually super-Eddington. For example, a solar mass star disrupted around a $10^6\,{\rm M}_\odot$ BH will have a peak fallback rate that is ∼100 times the Eddington rate, and the fallback rate should remain above Eddington for a few fallback times. Hydrodynamic simulations of the early stages of disc formation in a TDE suggest that as much as 20 per cent of the returning stream may actually cross the horizon through an accretion flow; however, the current library of published simulations is yet to cover a substantial range of the TDE parameter space and the effects of magnetism have largely been ignored in long-term simulations (Ramirez-Ruiz & Rosswog 2009; Guillochon, Manukian & Ramirez-Ruiz 2014; Shiokawa et al. 2015; Bonnerot et al. 2016; Hayasaki, Stone & Loeb 2016; Liptai et al. 2019; Bonnerot & Lu 2020; Bonnerot, Lu & Hopkins 2021; Curd 2021; Andalman et al. 2022; Steinberg & Stone 2022).

The exact nature of the accretion disc structure is still uncertain, but previous works have applied global general relativistic radiation magnetohydrodynamics (GRRMHD) accretion disc simulations to model the accretion flow (Dai et al. 2018; Curd & Narayan 2019). The emission properties of TDEs are possibly described by thick accretion discs (Dai et al. 2018; Curd & Narayan 2019). In particular, magnetically arrested discs (or MADs; Narayan, Igumenshchev & Abramowicz 2003) around spinning BHs produce powerful jets and have emission properties remarkably similar to that of *Swift* J1644 + 57 (Tchekhovskoy et al. 2014; Curd & Narayan 2019). For non-jetted TDEs, the 'standard and normal evolution' (or SANE) discs may be appropriate to describe X-ray TDEs, but the optical/UV component was uncertain in Curd & Narayan (2019) since it originated from the outer radius of the torus, which was initialized using an equilibrium torus model rather than from following the entire disc formation process in a TDE. SANE models may also apply to jetted TDEs, as a funnel region in super-Eddington accretion flows can result in highly energetic outflows capable of explaining even jetted events (Sądowski & Narayan 2015a; Coughlin & Begelman 2020). A numerical study of the radio/submillimetre emission from outflows driven by SANE super-Eddington accretion flows and its comparison with the radio emission in TDEs is thus well motivated.

In this work, we model the radio/submillimetre emission (via thermal synchrotron) from the outflows of super-Eddington accretion flows using GRRMHD simulations similar to those presented in Curd & Narayan (2019). However, in this work, we use a grid with more resolution in the jet and run the simulation substantially longer such that the outflow reaches radii similar to the emission scales for known radio TDEs (Alexander et al. 2020). We perform simulations of SANE accretion discs around BHs of mass $M_{\rm BH} = (5, 10) \times 10^6\,{\rm M}_\odot$ and a dimensionless BH spin of $a_* = (0, 0.5, 0.9)$ and measure the jet power and morphology across the parameter space. We perform general relativistic ray tracing (GRRT) of each model to produce spectra and images of the jet emission. We examine the viability of detecting and resolving the jet at 230 GHz, which is the frequency employed by the Event Horizon Telescope (EHT; Event Horizon Telescope Collaboration 2019). Based on our results, we suggest that the EHT or the next-generation EHT (ngEHT) could be suited for radio/submillimetre follow-up of TDEs. A direct probe of jet launching from super-Eddington accretion discs and radio/submillimetre emission in TDEs are both of significant interest and are expected to increase our understanding of BH accretion and the environment of BHs.

The paper is structured as follows. In Section 2, we motivate radio/submillimetre observations of nearby TDEs by computing the expected number of TDEs within $D < 60$ Mpc. In Section 3, we outline the numerical methods used in this work. In Section 4, we describe the accretion flow and outflow properties. In Section 5, we analyse GRRT radio/submillimetre spectra and images of each model and determine the viability of resolving the jets in each simulation with the EHT/ngEHT. We compare our results with current TDE radio observations in Section 6 and conclude in Section 7.

2 TDE RATES

In this section, we motivate follow-up observations of TDEs in the radio/submillimetre band by quantifying the number of TDEs in a given volume of the nearby universe assuming conservative TDE rates. We utilize methods described in Stone & Metzger (2016) and the interested readers should see their work for a detailed discussion of TDE rates. The number of possible TDEs per year grows rapidly at higher redshift since the number of BHs in an integrated volume of space varies as $N_{\rm BH}(D) \propto D^3$. Similarly, assuming estimates of the TDE rates are applicable broadly within the local universe (see Stone & Metzger 2016; Pfister et al. 2020), we can estimate the number of TDEs per year within a finite distance so long as we know the mass-dependent TDE rate of a given BH [$\Gamma(M_{\rm BH})$] as well as the BH mass function (BHMF, $\widetilde{\phi}(M_{\rm BH})$). The BHMF varies at larger cosmic distance, but here we consider only the local universe ($z < 0.1$), where the BHMF is essentially redshift independent.

We make use of the BHMF adopted by Stone & Metzger (2016) to estimate the volumetric TDE rate. See their work for an in-depth definition. To estimate the BHMF, we first define the R band luminosity (L_R) function of the galaxy by assuming it follows the Schechter function (Schechter 1976):

$$\widetilde{\phi}(L_R){\rm d}L_R = \widetilde{\phi}_* \left(\frac{L_R}{L_*}\right)^{-1.1} \exp(-L_R/L_*){\rm d}L_R, \qquad (2)$$

where $\widetilde{\phi}_* = 4.9 \times 10^{-3} h_7^3\,{\rm Mpc}^{-3}$ and $L_* = 2.9 \times 10^{10} h_7^{-2} L_\odot$. Here, $h_7 = 1$ is the normalized Hubble constant. Combining the above Schechter function with the Faber–Jackson law, $\sigma \approx 150\,{\rm km\,s^{-1}} (L_R/10^{10} L_\odot)^{1/4}$, with the McConnell & Ma (2013) calibration of the $M_{\rm BH}$–σ relation, we arrive at the BHMF (left-hand

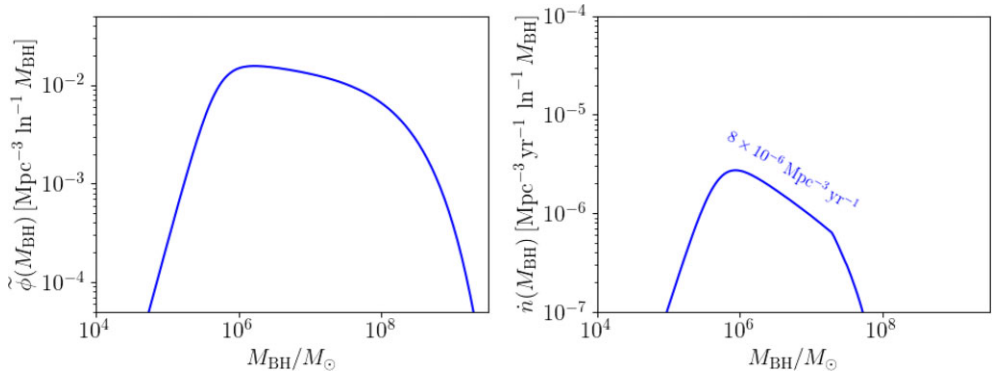

Figure 1. Here, we show the BHMF as calculated in the text (left-hand panel). We then show the volumetric TDE rate (right-hand panel). The text above the curve shows the TDE rate when the curve is integrated over BH mass.

panel in Fig. 1):

$$\widetilde{\phi}(M_{\rm BH})d\ln M_{\rm BH} = 2.56\widetilde{\phi}_* f_{\rm occ}\left(\frac{M_{\rm BH}}{10^8\,{\rm M}_\odot}\right)^{-1.07} \times \exp\left(-0.647\left(\frac{M_{\rm BH}}{10^8\,{\rm M}_\odot}\right)\right) d\ln M_{\rm BH}. \quad (3)$$

Here, $f_{\rm occ}$ is the occupation fraction, which accounts for the expectation that lower-mass galaxies may not host a SMBH at their centre. Following Stone & Metzger (2016), we define the occupation fraction as:

$$f_{\rm occ} = \begin{cases} 0.5\tanh\left[\ln\left(\frac{M_{\rm bulge}}{M_c}\right)\times 2.5^{8.9-\log_{10}(M_c/{\rm M}_\odot)}\right] + 0.5, & M_{\rm bulge} < 10^{10}\,{\rm M}_\odot \\ 1. & M_{\rm bulge} > 10^{10}\,{\rm M}_\odot \end{cases}$$

Here, M_c is a parameter determining the bulge mass below which the occupation fraction turns over and begins to approach zero as illustrated in Stone & Metzger (2016, fig. 7). We relate $M_{\rm bulge}$ to the BH mass with the $M_{\rm BH}$–$M_{\rm bulge}$ relation from McConnell & Ma (2013). As was noted by Stone & Metzger (2016), the value of $M_c = 10^{8.5}\,{\rm M}_\odot$ is the most likely case, so we fix $M_c = 10^{8.5}\,{\rm M}_\odot$ in our analysis.

We also account for the impact of different mass stars on the TDE rate by incorporating the Kroupa initial mass functions (IMF):

$$\chi_{\rm Kro} = \frac{{\rm d}N_*}{{\rm d}M_*} \propto \begin{cases} (M_*/M_\odot)^{-1.3}, & 0.08 < (M_*/M_\odot) < 0.5 \\ (M_*/M_\odot)^{-2.3}, & 0.5 < (M_*/M_\odot) < 1. \end{cases} \quad (4)$$

Note that we have followed Stone & Metzger (2016) and only assume stars in the range of $0.08 - 1\,{\rm M}_\odot$ are accounted for. This is reasonable particularly if we are considering older galaxies where high mass stars would have already evolved and died. We normalize the IMF such that $\int \chi_{\rm Kro}{\rm d}M_* = 1$.

For the TDE rate, $\Gamma_{\rm TDE}(M_{\rm BH})$, we use the upper limit estimate from Stone & Metzger (2016):

$$\Gamma_{\rm S16} = 2.9\times10^{-5}\,{\rm yr}^{-1}\left(\frac{M_{\rm BH}}{10^8\,{\rm M}_\odot}\right)^{-0.404}. \quad (5)$$

This estimate comes from core/cusp galaxies using a sample of roughly 200 objects. We note that the TDE rate can be increased in galaxies with denser stellar cores (see Pfister et al. 2020, for more details). However, in this work, we restrict ourselves to conservative estimates.

We infer the volumetric TDE rate as a function of BH mass accounting for both the distribution of stars and the fact that some stars will get swallowed and do not contribute to the TDE rate. Therefore, the volumetric TDE rate as a function of BH mass would be:

$$\dot{n}(M_{\rm BH}) = \int_{M_{*,\rm min}}^{M_{*,\rm max}} \Gamma(M_{\rm BH}, M_*)\widetilde{\phi}(M_{\rm BH})\chi_{\rm Kro}{\rm d}M_*. \quad (6)$$

where $\Gamma(M_{\rm BH}, M_*)$ is the TDE rate which is given by equation (5). We account for cases where the star is swallowed by the BH by setting $\Gamma(M_{\rm BH}, M_*) = 0$ if $R_{\rm t} < r_H$, where $r_{\rm H}$ is the horizon radius of the BH, for the star at the given BH mass. We show the volumetric TDE rate in the right-hand panel in Fig. 1 for $M_c = 10^{8.5} M_\odot$ and $\Gamma_{\rm S16}$. The text above the curve shows the integral $\dot{n} = \int \dot{n}(M_{\rm BH})d\ln M_{\rm BH}$ which is the total volumetric TDE rate. Lower cutoff masses for the occupation fraction can significantly increase the TDE rate, but the greatest enhancement comes from assuming that denser stellar cores are present.

To estimate the number of TDEs occurring within a closed volume in a finite amount of time, we use the total volumetric TDE rate, which is constant in time, to obtain:

$$N_{\rm TDE} = \frac{4}{3}\pi D^3 \dot{n}\Delta t, \quad (7)$$

where D is the distance in Mpc and Δt is the total time in years. Fig. 2 shows the TDE rates given a number of years (1 and 10 yr of observation).

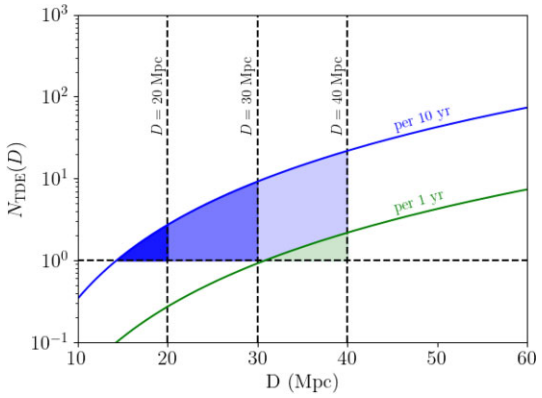

Figure 2. Here, we estimate the number of total TDEs expected given a limiting observable distance per year (green line) and per 10 yr (blue line). The shaded regions denote the range of parameter space where the expected number of TDEs in 1 yr (green) and 10 yr (blue) exceeds 1. We use a different shade where $D <= 20$, 30, and 40 Mpc to illustrate the impact of increasing the maximum distance by only 10 Mpc.

The vertical lines in Fig. 2 show the effect on the number of observable TDEs for a maximal observing distance. Even a modest maximum observing distance of $D < 20$ Mpc would provide 2–3 TDEs per decade while extending this range to $D < 40$ Mpc would lead to nearly 2 TDEs per year. Assuming these flares are captured by other survey telescopes, such as the Large Synoptic Survey Telescope (Ivezić et al. 2019), which is expected to lead to many more TDE detections in the coming years (Bricman & Gomboc 2020), radio/submillimetre follow-up of several TDEs may be possible. We note that we have assumed full sky coverage in our analysis, which is unrealistic, but our calculations demonstrate how the TDE rate varies with distance in order to quantify how beneficial the detector sensitivity may be. In the following sections, we, for the first time, attempt to quantify the observability of the radio/submillimetre emission from outflows launched by a super-Eddington accretion discs with mass accretion rates similar to the peak accretion rate in TDEs.

3 NUMERICAL METHODS

The simulations presented in this work were performed using the GRRMHD code KORAL (Sądowski et al. 2013, 2014; McKinney et al. 2014; Sądowski et al. 2017), which solves the conservation equations in a fixed, arbitrary space time using finite-difference method. We solve the following conservation equations:

$$(\rho u^{\mu})_{;\mu} = 0, \tag{8}$$

$$(T^{\mu}_{\nu})_{;\mu} = G_{\nu}, \tag{9}$$

$$(R^{\mu}_{\nu})_{;\mu} = -G_{\nu}, \tag{10}$$

where ρ is the gas density in the comoving fluid frame, u^{μ} is the components of the gas four-velocity as measured in the 'lab frame', T^{μ}_{ν} is the MHD stress-energy tensor in the 'lab frame':

$$T^{\mu}_{\nu} = (\rho + u_g + p_g + b^2)u^{\mu}u_{\nu} + \left(p_g + \frac{1}{2}b^2\right)\delta^{\mu}_{\nu} - b^{\mu}b_{\nu}, \tag{11}$$

R^{μ}_{ν} is the stress-energy tensor of radiation, and G_{ν} is the radiative four-force, which describes the interaction between gas and radiation (Sądowski et al. 2014). Here u_g and $p_g = (\gamma_g - 1)u_g$ are the internal energy and pressure of the gas in the comoving frame (linked by adiabatic index γ_g), and b^{μ} is the magnetic field four-vector, which is evolved following the ideal MHD induction equation (Gammie, McKinney & Tóth 2003). In the KORAL simulations, we assume a single-temperature plasma where the ion temperature ($T_{\rm i}$) and the electron temperature ($T_{\rm e}$) are identical. This description is adequate in the optically thick regions where collisions are common, but may not be accurate in the extended jet where the gas density is substantially lower (Liska et al. 2022). We also assume that the electrons follow a thermal distribution, which is another caveat in the initial KORAL simulations since internal shocks in the jet are expected to accelerate electrons into a non-thermal distribution. Magnetic reconnection events in the disc/wind may also produce regions where a non-thermal electron population exists, but we do not account for the possibility of these effects.

The radiative stress-energy tensor is obtained from the evolved radiative primitives, i.e. the radiative rest-frame energy density and its four velocity following the M1 closure scheme modified by the addition of radiative viscosity (Sądowski et al. 2013, 2015).

The opposite signs of G_{ν} in the conservation equations for gas and radiation stress-energy (equations 9 and 10) reflect the fact that the gas–radiation interaction is conservative, i.e. energy and momentum are transferred between gas and radiation (see Sądowski et al. 2017, for more details). We include the effects of absorption and emission via the electron scattering opacity ($\kappa_{\rm es}$), free–free absorption opacity ($\kappa_{\rm a}$), and bound-free absorption opacity through the Sutherland Dopita model (Sutherland & Dopita 1993) and assume a solar metal abundance for the gas. We also include the effects of thermal synchrotron and Comptonization (Sądowski & Narayan 2015b; Sądowski et al. 2017).

The simulations presented in this work are conducted in 2D $r - \vartheta$ coordinates, and we implement the mean-field dynamo model described in Sądowski et al. (2015) to sustain the magnetic field throughout the simulation.

3.1 Basic dynamics

A star which has been captured by an SMBH will be disrupted when it can no longer be held together by its self-gravity. This occurs at radii less than the tidal radius:

$$R_{\rm t}/r_g = 47\left(\frac{M_{\rm BH}}{10^6\,{\rm M}_{\odot}}\right)^{-2/3}\left(\frac{M_*}{M_{\odot}}\right)^{-1/3}\left(\frac{R_*}{R_{\odot}}\right). \tag{12}$$

It is common to describe the disruption in terms of the impact parameter, β, which is defined as the ratio between the tidal radius and pericentre separation such that $\beta \equiv R_{\rm t}/R_{\rm p}$.

The pericentre separation at which a full disruption of the star is sensitive to the stellar composition since the compactness of the star effects how easily it is disrupted. For zero-age main sequence stars, those described by a $\gamma = 5/3$ polytrope are fully disrupted if $\beta \gtrsim 0.9$, while stars described by a $\gamma = 4/3$ polytrope must come within $\beta \gtrsim 2$ (Guillochon & Ramirez-Ruiz 2013; Mainetti et al. 2017). Golightly, Nixon & Coughlin (2019) demonstrated that the pericentre separation required for evolved stars is even smaller (sometimes greater than $\beta = 3$ based on their findings) as the core is no longer hydrogen dominated due to its compactness. For our purposes, we assume a ZAMS star with a $\gamma = 5/3$ polytrope was disrupted for simplicity.

If hydrodynamical forces are neglected, then the change in the specific binding energy of the fluid in the star as a result of the tidal interaction can greatly exceed the internal binding energy of the star (Rees 1988). As a result, a spread in binding energy is imparted on the stellar material. Stone et al. (2013) find that the spread in orbital energy $\Delta\epsilon$ is insensitive to β since the energy is essentially frozen in at the tidal radius. This spread is then given by:

$$\Delta\epsilon \approx 4.3\times10^{-4}\left(\frac{M_{\rm BH}}{10^6\,{\rm M}_{\odot}}\right)^{1/3}\left(\frac{M_*}{M_{\odot}}\right)^{2/3}\left(\frac{R_*}{R_{\odot}}\right)^{-1}c^2. \tag{13}$$

The orbital binding energy of the most/least bound material is given by $\epsilon_{\rm mb} = \epsilon_* - \Delta\epsilon/2$ and $\epsilon_{\rm lb} = \epsilon_* + \Delta\epsilon/2$. Here, ϵ_* is the initial orbital binding energy of the star. For parabolic orbits, which have $\epsilon_* = 0$, the spread in binding energy leads to half of the mass remaining bound and the other half being ejected. In this work, we assume the star was disrupted on a parabolic orbit since the majority of TDEs will be of such stars.

The spread in binding energy is one of the most crucial parameters that defines the TDE evolution. In particular, the fallback time (equation 1) and the peak mass fallback rate:

$$\frac{\dot{M}_{\rm fb,peak}}{\dot{M}_{\rm Edd}} \approx 133\left(\frac{M_{\rm BH}}{10^6\,{\rm M}_{\odot}}\right)^{-3/2}\left(\frac{M_*}{M_{\odot}}\right)^{2}\left(\frac{R_*}{R_{\odot}}\right)^{-3/2}, \tag{14}$$

are direct consequences of the spread in binding energy.

3.2 Definitions

In this section, we discuss the units adopted throughout the text and provide brief descriptions of quantities used to study the KORAL simulation data.

Throughout this work, we use gravitational units to describe physical parameters. For distance, we use the gravitational radius $r_g \equiv GM_{BH}/c^2$ and for time, we use the gravitational time $t_g \equiv GM_{BH}/c^3$, where M_{BH} is the mass of the BH. Often, we set $G = c = 1$, so the above relations would be equivalent to $r_g = t_g = M_{BH}$.[1] Occasionally, we restore G and c when we feel it helps to keep track of physical units.

We adopt the following definition for the Eddington mass accretion rate:

$$\dot{M}_{Edd} = \frac{L_{Edd}}{\eta_{NT} c^2}, \tag{15}$$

where $L_{Edd} = 1.25 \times 10^{38} (M_{BH}/M_\odot)$ erg s^{-1} is the Eddington luminosity, η_{NT} is the radiative efficiency of a thin disc around a BH with spin parameter a_* (which is often referred to as the Novikov–Thorne efficiency):

$$\eta_{NT} = 1 - \sqrt{1 - \frac{2}{3 r_{ISCO}}}, \tag{16}$$

and $r_{ISCO} = 3 + Z_2 - \sqrt{(3 - Z_1)(3 + Z_1 + 2Z_2)}$ is the radius of the Innermost Stable Circular Orbit (Novikov & Thorne 1973) in the Kerr metric, where $Z_1 = 1 + (1 - a_*^2)^{1/3} \left((1 + a_*)^{1/3} + (1 - a_*)^{1/3}\right)$ and $Z_2 = \sqrt{3a_*^2 + Z_1^2}$. For $a_* = 0$, 0.5, and 0.9, the efficiency is $\eta_{NT} =$ 5.72 per cent, 8.21 per cent, and 15.58 per cent.

We compute the net mass inflow rate as:

$$\dot{M}(r) = -2\pi \int_0^\pi \sqrt{-g} \rho u^r d\vartheta. \tag{17}$$

We treat the accretion of mass onto the BH as this integral taken at the horizon r_H.

We estimate the electron scattering photosphere location for an observer at infinity along the direction (ϑ) by integrating the optical depth radially inward from the outer boundary of the grid. Far from the BH, the curvature of space time is negligible, so we simply integrate at constant (ϑ) in the 'lab frame':

$$\tau_{es}(r) = \int_r^{R_{max}} \frac{\rho \kappa_{es}}{c} \left(u^t - u^r\right) \sqrt{g_{rr}} dr', \tag{18}$$

where $\kappa_{es} = 0.2(1 + X)\kappa_{KN}$ cm^2 is the electron scattering opacity, X is the Hydrogen mass-fraction, which is assumed to be the Solar abundance $X_\odot = 0.7381$, κ_{KN} is the Klein–Nishina correction factor for thermal electrons (Sądowski et al. 2017), and R_{max} is the radius corresponding to the outer boundary of the grid. For the gas and radiation temperatures in the simulations presented here, the Klein–Nishina correction is negligible and the electron scattering opacity is essentially the Thomson opacity. In this work, we choose the location of the photosphere as the $\tau_{es} = 1$ surface.

We define the accretion flow as three distinct regions (disc, wind, and jet) based on the total energy via the Bernoulli parameter. We also make use of the electron scattering opacity, τ_{es}, to determine whether the region of the fluid under consideration is optically thin or thick. In optically thick regions, i.e. ($\tau_{es} \geq 1$), the radiation is advected with the flow and can contribute to acceleration of the gas so we treat it as contributing to the Bernoulli parameter. Meanwhile, in optically thin regions, i.e. ($\tau_{es} < 1$), we assume that only the MHD components are relevant to the total gas energy. We modify the Bernoulli definition used in Curd & Narayan (2019) to include optically thin regions where the interaction between gas and radiation can be neglected via:

$$\mathrm{Be} = \begin{cases} -\dfrac{(T^t{}_t + R^t{}_t + \rho u^t)}{\rho u^t}, & \text{(optically thick)} \\ -\dfrac{(T^t{}_t + \rho u^t)}{\rho u^t}, & \text{(optically thin)} \end{cases} \tag{19}$$

The 'disc' is made up of bound gas with Be < 0. This constitutes both the inner accretion disc and the large mass reservoir of the initial torus. Both the 'wind' and 'jet' are unbound and are generally radially out flowing. The wind is defined as any fluid with $0 <$ Be ≤ 0.05. The jet is any fluid with Be > 0.05. This choice of cutoff for wind vs. jet is based on the velocity at infinity (v_∞), with the wind having $v_\infty \lesssim 0.3c$ and the jet having $v_\infty \gtrsim 0.3c$. It is worth noting that this choice assumes that gas at small radii will not lose/gain energy as it travels outward, which is not guaranteed to be the case outside of steady state regions. A fraction of the positive Bernoulli gas in the simulation domain could remain bound to the BH such as in Coughlin, Quataert & Ro (2018); however, the Bernoulli is still a useful approximate definition to characterize the outflow based on energy. We make use of the Bernoulli parameter to find the opening angle of the jet, i.e. we define $\vartheta_{jet}(r)$ such that:

$$\mathrm{Be}(r, \vartheta_{jet}(r)) = 0.05. \tag{20}$$

We visualize the gas density, optical depth, and Bernoulli in simulation `m5a0.0-HR` (described later in the text) in Fig. 3. At small scales, the disc is clearly separated from the funnel/outflow region based on our definition. In addition, the wind initially constitutes a small angular region of the funnel and is clearly a higher density gas than the jet component. At large scales, the jet is a lower density region, which is hugged by the higher density wind.

The total luminosity (the net energy flux) is computed as:

$$L_{net}(r) = -2\pi \int_0^\pi \sqrt{-g}(T^r{}_t + R^r{}_t + \rho u^r) d\vartheta, \tag{21}$$

where we integrate the radial flux of energy carried by gas plus magnetic field ($T^r{}_t$) and radiation ($R^r{}_t$), and subtract out the rest-mass energy (ρu^r, since it does not lead to observational consequences for an observer at infinity). When computed at the BH horizon, equation (21) gives the total energy extracted from the accretion flow so we define $L_{tot} = L_{net}(r_H)$. We also compute the total energy outflowing in the wind and jet as:

$$L_{MHD}(r) = -2\pi \int_0^\pi \sqrt{-g}(T^r{}_t + \rho u^r) d\vartheta. \tag{22}$$

We compute energy outflow in the wind at $r = 1000\, r_g$ by using equation (22), but we only sum energy outflows where the gas is unbound, outflowing, and non-relativistic (or $0 <$ Be < 0.05 and $u^r > 0$). A similar choice is made to compute the total energy outflowing in the jet at $r = 1000\, r_g$ but we use the criterion that energy is only summed where Be ≥ 0.05 and $u^r > 0$. Note that at $1000\, r_g$, the wind and jet are in an optically thin region so the Bernoulli is computed without the radiation energy density included.

The radiative bolometric luminosity is given by:

$$L_{bol}(r) = -2\pi \int_0^\pi \sqrt{-g} R^r{}_t d\vartheta, \tag{23}$$

which gives the flux of radiation energy through a surface at a given radius. In this work, we measure the flux through a sphere at $r =$

[1] For a BH mass of 10^6 M$_\odot$, the gravitational radius and time in CGS units are $r_g = 1.48 \times 10^{11}$ cm and $t_g = 4.94$ s, respectively.

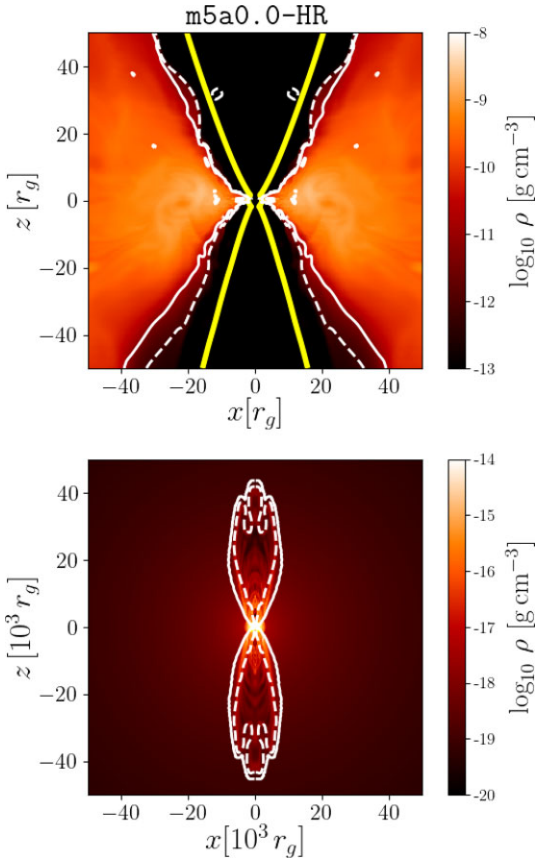

Figure 3. Here, we visualize an evolved disc/jet. We show the gas density (colours) as well as the $\tau_{es} = 1$ (yellow line), Be = 0 (white line), and Be = 0.05 (dashed white line) contours. Note that we reflect the data about the x-axis for visualization purposes, but the simulation was run in 2D $r - \vartheta$ coordinates. In the top panel, we focus on the inner accretion disc and funnel region to illustrate the separation of the disc (region inside the solid white lines) from the wind (region between solid and dashed white lines) and the jet (region inside of dashed lines). At large scales, the wind (region between solid and dashed white lines) is clearly delineated from the jet (region inside of dashed lines) and the initial bound atmosphere (region outside of solid white lines).

$5000\,r_g$, which lies beyond the outer radius of the initial torus, and define $L_{5000} = L_{\rm bol}(5000\,r_g)$. We assume rays crossing the surface reach a distant observer.

We define the total, wind, jet, and radiation efficiencies as:

$$\eta_{\rm tot} = \frac{1}{\dot{M}} L_{\rm net}(r = r_H), \tag{24}$$

$$\eta_{\rm wind} = \frac{1}{\dot{M}} L_{\rm MHD}(r = 1000\,r_g, 0.05 > {\rm Be} > 0, u^r > 0), \tag{25}$$

$$\eta_{\rm jet} = \frac{1}{\dot{M}} L_{\rm MHD}(r = 1000\,r_g, {\rm Be} \geq 0.05, u^r > 0), \tag{26}$$

and

$$\eta_{\rm rad} = \frac{1}{\dot{M}} L_{\rm bol}(r = 5000\,r_g), \tag{27}$$

In each case, positive values correspond to energy being extracted from the system.

The magnetic flux is computed as:

$$\Phi(r) = -\pi \int_0^\pi \sqrt{-g} |B^r(r)| {\rm d}\vartheta, \tag{28}$$

where B^r is the radial component of the magnetic field. We quantify the magnetic field strength at the BH horizon through the normalized magnetic flux parameter (Tchekhovskoy, Narayan & McKinney 2011):

$$\phi_{\rm BH} = \frac{\Phi(r_H)}{\sqrt{\dot{M}(r_H)}}. \tag{29}$$

For geometrically thick discs, the MAD state is achieved once $\phi_{\rm BH} \sim 40$–50 (see e.g. Tchekhovskoy et al. 2011; Tchekhovskoy, McKinney & Narayan 2012).

To characterize the magnetic field, we define the magnetic pressure ratio:

$$\beta_t \equiv \frac{(p_{\rm gas} + p_{\rm rad})}{p_{\rm mag}}, \tag{30}$$

(distinguished from the impact parameter β) which is used to define the pressure ratio in optically thick regions where the radiation is dynamically important. Note that we also make use of the ratio between the gas and magnetic pressure:

$$\beta_g \equiv \frac{p_{\rm gas}}{p_{\rm mag}}, \tag{31}$$

which is used to characterize the optically thin jet.

We quantify the resolution of the fastest growing mode of the magnetorotational instability (MRI; Balbus & Hawley 1991) by computing the quantity:

$$Q_\vartheta = \frac{2\pi}{\Omega {\rm d}x^\vartheta} \frac{|b^\vartheta|}{\sqrt{4\pi\rho}}, \tag{32}$$

where ${\rm d}x^\vartheta$ (the grid cell in polar coordinate ϑ) and b^ϑ (the ϑ component of the magnetic field) are both evaluated in the orthonormal frame, Ω is the angular velocity, and ρ is the gas density. Numerical studies of the MRI have shown that values of Q_ϑ in excess of at least 10 are needed to resolve the fastest growing mode (Hawley, Guan & Krolik 2011). As we are considering 2D simulations in $r - \vartheta$, we do not consider the ϕ MRI quality factor. Throughout each simulation, we find the quality factor $Q_\vartheta > 10$ at the mid-plane for $r < 50\,r_g$.

3.3 Numerical models/initial conditions

The domain outside of the gas torus is initialized with a low density, hot gas with a density maximum at the BH horizon of:

$$\rho_{\rm atm,max} = 4.5 \times 10^{-8} \left(\frac{M_{\rm BH}}{M_\odot}\right)^{-1} [\mathrm{g\,cm^{-3}}]. \tag{33}$$

The gas temperature at the BH horizon is set to $T_{\rm atm,\,max} = 10^{11}$ K. We assume that the atmosphere follows a profile similar to a spherical accretion flow (Bondi 1952) and set the gas density in the atmosphere using a radial profile $\rho_{\rm atm} \propto r^{-3/2}$ while the internal energy varies as $u_{g,\rm atm} \propto r^{-5/2}$. The radiation in the atmosphere is initialized with a radiation temperature of $5 \times 10^4 (M_{\rm BH}/M_\odot)$ K everywhere, which ultimately defines an atmosphere with negligible radiation energy initially.

To initialize the torus, we assume that the stream rapidly circularized and formed an accretion flow. It is important to note that this model assumes that the circularization process happens on a timescale that is much shorter than the fallback time. We also assume that angular momentum and binding energy are conserved, which allows for simple initial conditions of the initial gas torus to be defined.

Using these inputs, we follow the method described in Kato, Mineshige & Shibata (2004) to initialize the simulation domain with an equilibrium torus, which has its angular momentum vector

Table 1. Simulation parameters and properties of the three simulations presented in this work. We specify the BH mass ($M_{\rm BH}$), average accretion rate ($\langle \dot{M} \rangle$), spin of the BH (a_*), average magnetic flux ($\langle \phi_{\rm BH} \rangle$), total efficiency computed at r_H ($\eta_{\rm tot}$), wind and jet efficiency computed at $1000\,r_g$ ($\eta_{\rm wind}$ and $\eta_{\rm jet}$), radiative efficiency computed at $5000\,r_g$ ($\eta_{\rm rad}$), simulation duration in t_g, grid resolution, inner and outer edges of the initial torus, and the inner and outer radial boundaries of the simulation box. Note that the accretion rate ($\langle \dot{M} \rangle$), magnetic flux ($\langle \phi_{\rm BH} \rangle$), and efficiencies ($\eta_{\rm tot}$, $\eta_{\rm wind}$, $\eta_{\rm jet}$ and $\eta_{\rm rad}$) are computed using time averages over the final $50,000\,t_g$ of each simulation.

	m5a0.0-HR	m5a0.5-HR	m5a0.9-HR	m10a0.0-HR	m10a0.5-HR	m10a0.9-HR
$M_{\rm BH}$ ($M_\odot$)	5×10^6	5×10^6	5×10^6	10^7	10^7	10^7
$\langle \dot{M} \rangle (\dot{M}_{\rm Edd})$	∼11	∼11	∼11	∼12	∼16	∼25
a_*	0	0.5	0.9	0	0.5	0.9
$\langle \phi_{\rm BH} \rangle$	4.3	7.6	5.8	4.5	4.2	5.8
$\eta_{\rm tot}$	4.00 per cent	7.19 per cent	14.17 per cent	4.29 per cent	6.42 per cent	13.23 per cent
$\eta_{\rm wind}$	0.23 per cent	0.52 per cent	0.88 per cent	0.10 per cent	0.22 per cent	0.72 per cent
$\eta_{\rm jet}$	0.38 per cent	0.96 per cent	2.75 per cent	0.24 per cent	0.63 per cent	1.15 per cent
$\eta_{\rm rad}$	3.33 per cent	4.64 per cent	12.34 per cent	3.76 per cent	4.39 per cent	5.48 per cent
$R_0 (r_g)$	20	20	20	20	20	20
Duration (t_g)	83 000	83 000	83 000	83 000	83 000	81 200
$N_r \times N_\vartheta$	640 × 256	640 × 256	640 × 256	640 × 256	640 × 256	640 × 256
$R_{\rm in} (r_g)/R_{\rm out} (r_g)$	10/3000	10/3000	10/3000	10/3000	10/3000	10/3000
$R_{\rm min} (r_g)/R_{\rm max} (r_g)$	$1.1/10^5$	$1.1/10^5$	$1.1/10^5$	$1.1/10^5$	$1.1/10^5$	$1.1/10^5$

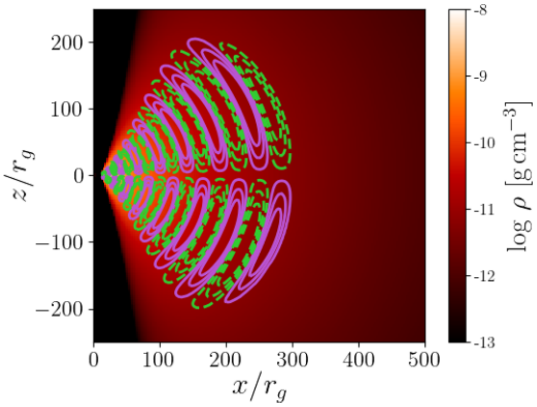

Figure 4. Here, we show the initial torus configuration for model m5a0.0-HR in terms of the gas density (colours) and vector potential A_ϕ (contours). The solid purple (dashed green) lines denote positive (negative) vector potential.

aligned with the BH spin vector. We set the radius of the density maximum of the torus (R_0, see Table 1) to occur at $R_{\rm circ} = 2R_p$ and the binding energy is initialized using a constant angular momentum torus with $l = \sqrt{R_{\rm circ}}$ and $\epsilon = \epsilon_{\rm mb}$. This results in a tenuously bound, geometrically thick torus where the inner edge of the torus ($R_{\rm in}$) is smaller than R_0 and the outer edge ($R_{\rm out}$) is at 1000s of $r_{\rm g}$ (see values in Table 1). In each model, our choice of density maximum results in a late-time accretion rate of $\gtrsim 11\,\dot{M}_{\rm Edd}$.

The magnetic field is initialized in terms of the vector potential (A_ϕ) using multiple field loops with varying polarity across the mid-plane and in radius (see Fig. 4). This guarantees that the accretion disc remains at a low magnetic flux throughout. Without this initialization, the chance advection of a large poloidal field loop towards the BH horizon can drive the disc towards a MAD state, which we cannot accurately simulate in 2D. The magnetic field is normalized such that the maximum pressure ratio $\beta_{t,\rm max} \equiv (p_{\rm gas,max} + p_{\rm rad,max})/p_{\rm mag,max} = 33$. This choice of magnetic pressure is somewhat arbitrary, but is sufficient to resolve MRI in the initial torus. As the simulations in this work are performed in spherical $r - \vartheta$ coordinates, we employ a mean field dynamo, which mimics the dynamo processes that naturally take place in full 3D simulations and prevent the magnetic flux from weakening throughout the simulation.

Similar to Narayan et al. (2022), we use a grid that has more cells both near the poles to resolve the outflow and in the mid-plane to resolve the disc. We use the coordinate transformation from spatial simulation 'code coordinates' (x_1, x_2) to Kerr–Schild grid coordinates (r, ϑ) introduced in Ressler et al. (2017). The simulation grid is logarithmically spaced in radius r, while the polar angle ϑ is a function of both x_1 and x_2, designed to concentrate resolution in the jet and disc regions.

We set the following parameters for the grid, where we use the same notation, as in Ressler et al. (2017, Appendix B). The hyperexponential break radius is set at $r_{\rm br} = R_{\rm max}$ such that the entire radial grid is spaced logarithmically. The collimation radii are $r_{\rm coll,\,jet} = 1000 r_{\rm g}$, $r_{\rm coll,\,disc} = 5r_+$, the decollimation radii are $r_{\rm decoll,\,jet} = r_{\rm decoll,\,disc} = 2r_+$. The power-law indices are $\alpha_1 = 1$, $\alpha_2 = 0.25$. The fraction of the angular resolution concentrated in the jet and disc are $f_{\rm jet} = 0.35$, $f_{\rm disc} = 0.4$. We 'cylindrify' cells close to the axis at small radii by expanding their size in ϑ (Tchekhovskoy et al. 2011; Ressler et al. 2017); the cylindrification radius $r_{\rm cyl} = 20 r_{\rm g}$ and $n_{\rm cyl} = 1$. This is an important step as it increases the minimum time-step of the simulation and increases the computational efficiency by nearly 2–3 times. The polar angle code coordinate x_2 extends from $x_{2,\,\rm min} = 10^{-5}$ to $x_{2,\,\rm max} = 1 - 10^{-5}$, where $x_2 = 0$ and 1 correspond to the two polar axes.

We set the resolution $N_r \times N_\vartheta$ such that the cells are roughly 1:1 in most of the simulation domain. We use modified Kerr–Schild coordinates with the inner edge of the domain inside the BH horizon. At the inner radial boundary ($R_{\rm min}$), we use an outflow condition, while at the outer boundary ($R_{\rm max}$), we use a similar boundary condition and in addition prevent the inflow of gas and radiation. Note that our choice of $R_{\rm min}$ is such that at least six cells in the computational domain lie inside of the horizon. At the polar boundaries, we use a reflective boundary. Furthermore, the inner two cells at the jet axis are not evolved and instead we copy the primitives from the third cell from the polar axis to bolster numerical stability. We employ a periodic boundary condition in azimuth. To maintain numerical stability, we introduce mass in highly magnetized regions of the simulation domain using a floor condition on the magnetization $\sigma \equiv b^2/\rho \leq 100$ throughout each simulation.

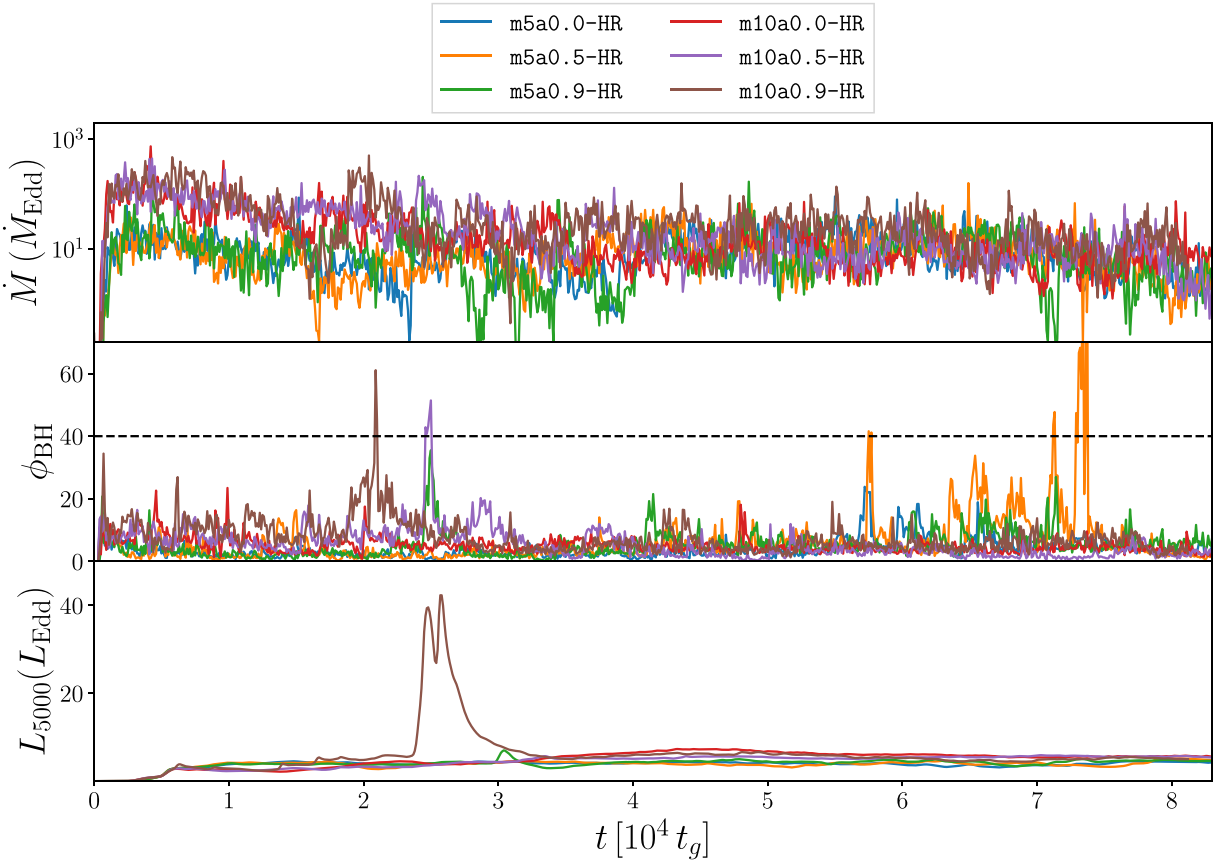

Figure 5. Here, we show the mass accretion rate (top), normalized magnetic flux at the BH horizon (middle), and bolometric luminosity (bottom) for each model. Also indicated is $\phi_{\rm BH} = 40$ (horizontal dashed line), which is approximately the magnetic flux at which a geometrically thick disc will enter the MAD state.

We identify the simulations by the BH mass in units of $m_6 = M_{\rm BH}/10^6\,{\rm M}_\odot$ and the dimensionless BH spin a_*. For instance, `m5a0.5-HR` corresponds to a BH mass of $5 \times 10^6\,{\rm M}_\odot$ with $a_* = 0.5$. See Table 1 for descriptions of each model.

4 RESULTS

4.1 Accretion flow properties

We show the accretion rate, magnetic flux at the BH horizon, and the luminosity of outgoing radiation computed directly from the KORAL data in Fig. 5. For each model in Fig. 5, the accretion rate does not remain at the initial accretion rate (e.g. $\sim$100 for `m10a0.0-HR`) and instead goes through phases of high and low accretion, eventually settling into a nearly steady-state accretion phase for $t \gtrsim 25\,000\,t_{\rm g}$. The magnetic flux in each simulation is generally $\phi_{\rm BH} \lesssim 5$, which is well below the limit for the MAD state ($\phi_{\rm BH} \gtrsim 40$).

There are occasional periods where a loop of poloidal magnetic field is advected towards the BH horizon and momentarily drives $\phi_{\rm BH}$ near the MAD limit. As indicated by the accretion rate, this does not disrupt the accretion flow (which typically occurs for strongly magnetized accretion flows at the MAD limit in 2D), but the Blandford–Znajek (Blandford & Znajek 1977) process will extract some spin energy from the BH and momentarily increase the jet power in the case of a spinning BH. The most extreme increase in $\eta_{\rm tot}$ due to the Blandford–Znajek process occurs in model `m10a0.9-HR` as $\phi_{\rm BH}$ around $t = 20\,000\,t_{\rm g}$ increases the total efficiency to $\eta_{\rm tot} \sim$ 110 per cent momentarily, which is to be expected in MAD accretion discs around rapidly rotating BHs (Curd & Narayan 2019). The effect of this is a brief order-of-magnitude increase in the escaping radiation roughly $5000\,t_g$ later due to the light crossing time between where we measure $\eta_{\rm tot}$ versus where we measure $L_{\rm bol}$. The two peaks in $L_{\rm bol}$ around $t = 25\,000\,t_{\rm g}$ are due to the increase in radiation flowing through the top and bottom jets crossing the $r = 5000\,r_g$ surface at different times.

The other models do not have as dramatic an increase in their efficiency or $L_{\rm bol}$, even during later spikes in $\phi_{\rm BH}$. These events are extremely short lived (lasting at most $100\,t_g$, which is the cadence at which we save snapshots of the simulations) and rare, so these deviations are not the driving factor in the energetics and jet evolution. Aside from the short increase in $L_{\rm bol}$ for model `m10a0.9-HR` at $t = 25\,000\,t_{\rm g}$, the escaping radiation is slightly super-Eddington at $L_{5000} \approx 3L_{\rm Edd}$.

Since each of the simulations has similar disc features, we focus on `m5a0.0-HR` to describe the inner accretion flow properties. Visualizations of the simulation data for `m5a0.0-HR` are shown in Fig. 6. The accretion disc is evidently thick and turbulent, with the turbulence being driven by MRI. The gas accretes onto the BH primarily along the equatorial plane. The flow is significantly turbulent even at relatively large radii. The turbulent structure of the velocity streamlines is in part the result of material near the BH gaining energy and being launched back into the disc. For such a low binding energy disc, small perturbations can lead to the material becoming unbound quite easily. Outflows driven by radiation and

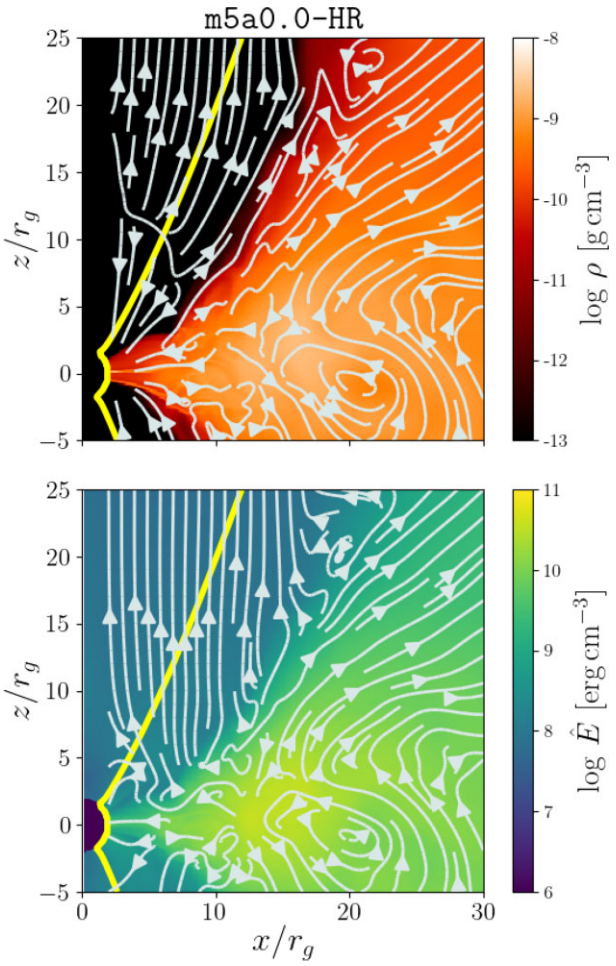

Figure 6. A zoomed-in view of the accretion flow and funnel of `m5a0.0-HR` at $t = 83\,000\,t_g$. The colours show the gas density (top) and radiation energy density (bottom). The streamlines indicate the fluid velocity (top) and radiative flux (bottom). We also indicate the photosphere ($\tau_{es} = 1$, yellow line).

Poynting flux are evident within ∼45° from the pole. For an in-depth description of the accretion flow of similar SANE models, see Curd & Narayan (2019).

To characterize the acceleration of gas in the jet, we compute the contributions to the energy flux in the Be > 0.05 region for the top jet. Namely, we compute the kinetic plus gravitational binding energy ($\dot{E}_{\rm kin+bind}$), internal ($\dot{E}_{\rm int}$), magnetic ($\dot{E}_{\rm mag}$), and radiative ($\dot{E}_{\rm rad}$) energy fluxes. The energy fluxes are computed as:

$$\dot{E}_{\rm kin+bind}(r) = -2\pi \int_0^{\vartheta_{\rm jet}(r)} \sqrt{-g}\,(\rho u^r u_t + \rho u^r)\,{\rm d}\vartheta, \tag{34}$$

$$\dot{E}_{\rm mag}(r) = -2\pi \int_0^{\vartheta_{\rm jet}(r)} \sqrt{-g}\,(b^2 u^r u_t - b^r b_t)\,{\rm d}\vartheta, \tag{35}$$

and

$$\dot{E}_{\rm rad}(r) = -2\pi \int_0^{\vartheta_{\rm jet}(r)} \sqrt{-g}\,R^r{}_t\,{\rm d}\vartheta, \tag{36}$$

respectively. We ignore the flux of gas internal energy since the gas is radiation pressure-dominated. We illustrate the acceleration of gas by radiation in model `m5a0.0-HR` in Fig. 7. For radii $50 \lesssim r/r_g \lesssim 5000$, we see a steady conversion of radiative flux to kinetic plus binding energy flux. However, the fraction of energy flux in the form of radiation in the jet begins to increase for $r \gtrsim 5000\,r_g$. We attribute

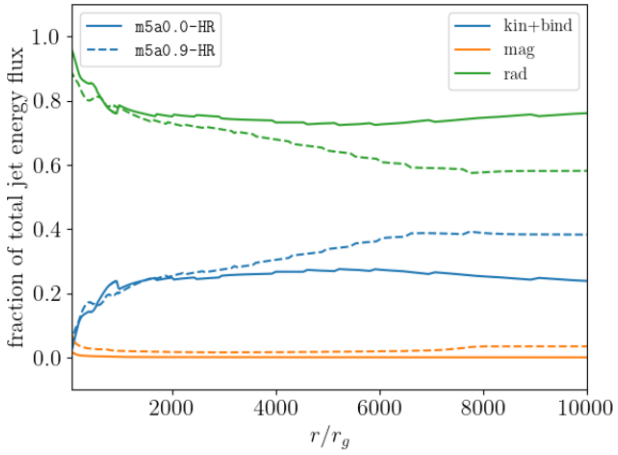

Figure 7. Here, we present the fraction of energy flux in the top jet for model `m5a0.0-HR` (solid lines) and `m5a0.9-HR` (dashed lines) in the form of radiation energy flux ($R^r{}_t$, green), kinetic plus gravitational binding energy flux ($\rho u^r u_t + \rho u^r$, blue), and magnetic energy flux ($b^2 u^r u_t - b^r b_t$, orange). The data have been time averaged over $t = 33\,000 - 83\,000\,t_g$. For radii $r \lesssim 5000 r_g$, we observe a continual conversion of radiation energy to kinetic and binding energy. Beyond roughly $5000\,r_g$, the fraction of energy flux in radiation steadily increases. This is likely due to a combination of dissipation of kinetic energy as well as the fact that the radiation is no longer forced to flow through the funnel for $r \gtrsim 3000\,r_g$ and can escape laterally. The magnetic energy flux in the jet also appears to increase with spin, which contributes to accelerating lower density gas along the jet axis.

this to two factors. First, there is some conversion of kinetic energy into thermal and radiation energy due to internal shocks within the jet (which we illustrate at the end of this section). In addition, there is also the fact that the radiation is no longer laterally confined by the funnel walls for $r \gtrsim 3000\,r_g$. Once the radiation can escape laterally, the radiation force supplied to gas along the jet axis declines. The fact that the fraction of radiation energy flux in the jet begins to climb for $r \gtrsim 5000\,r_g$ suggests that the optically thick gas is weakly accelerated by radiation at larger radii.

We present a snapshot of the jet resulting from the accretion flow in Fig. 8. Much of the radiation energy density is contained within the disc near the equatorial plane. Radiation is advected in with the accretion flow and escapes out through the funnel, driving a mildly relativistic outflow ($\gamma \lesssim 1.2$). As described in Sądowski & Narayan (2015a), this process occurs because optically thick gas flows from the disc into the funnel region and is subsequently accelerated by the radiation streaming through the funnel. The non-spinning BH model `m5a0.0-HR` reaches similar gas velocities in the jet as the models presented in Sądowski & Narayan (2015a), which were also of $a_* = 0$ BHs. The disc is radiation pressure-dominated, but contributions from radiation energy to the total pressure in the jet will be negligible due to the low-optical depth. However, the magnetic pressure can become quite large in the jet and sometimes exceeds the gas pressure within the jet. Some regions reach above the magnetization σ of unity. The map of the magnetization σ shows that it is primarily near the pole where the gas becomes strongly magnetized.

Despite maintaining $\phi_{\rm BH} \sim 4 - 7$ in each model, the spin $a_* > 0$ models each show increased jet power and relativistic ($\gamma > 2$) but low density outflows near the poles. We illustrate this for `m5a0.9-HR` in Fig. 9. We also note that the magnetic field strength is greater along the extended jet and, as a consequence, the jet is more magnetized in general as indicated by the extent of the $\sigma > 1$ region. The fractional energy flux profiles in model `m5a0.9-HR` (Fig. 7)

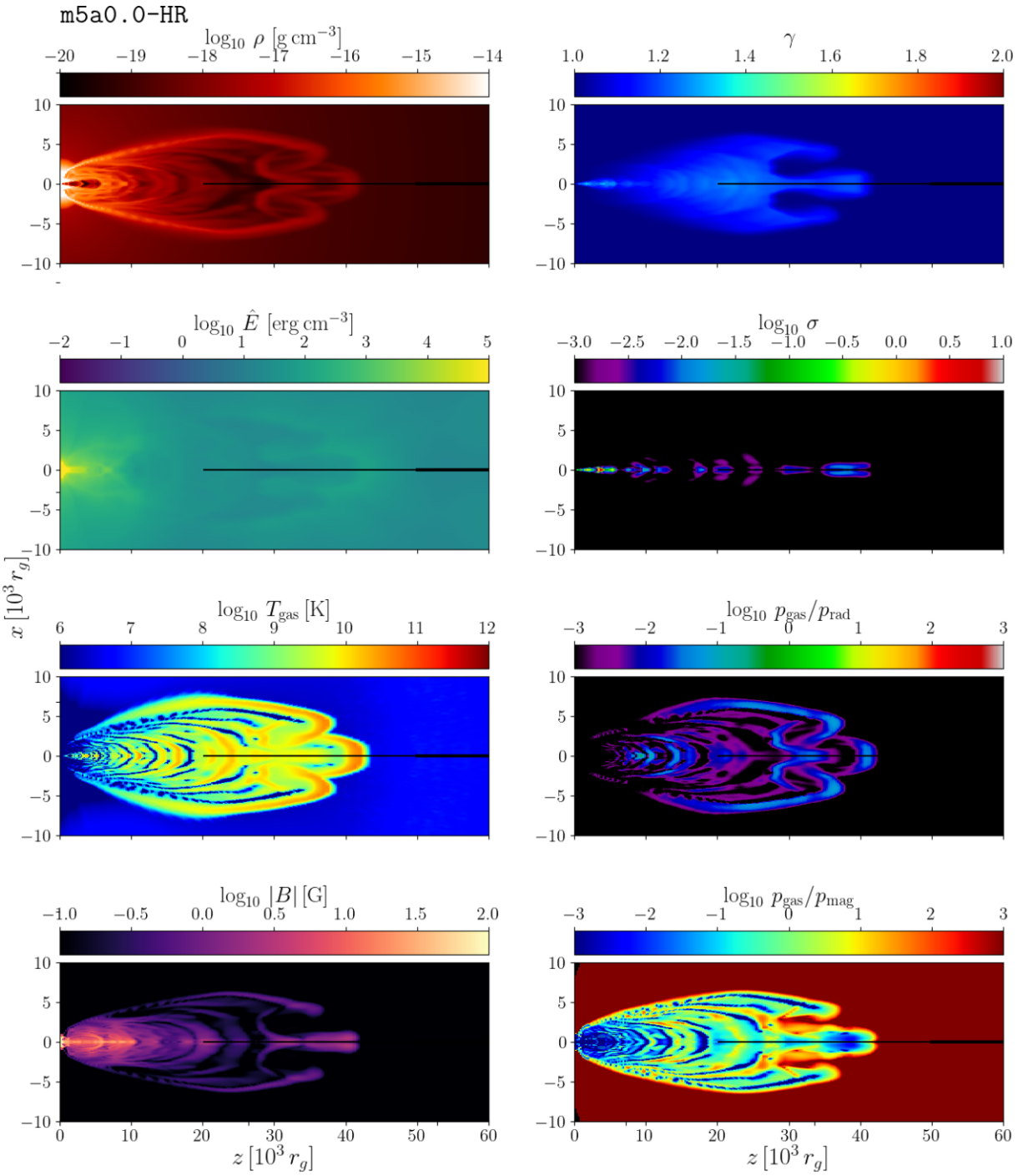

Figure 8. Here, we show a zoomed-out view of `m5a0.0-HR` at $t = 83,000\,t_g$. Note that we reflect the data about the x-axis for visualization purposes, but the simulation was run in 2D $r - \vartheta$ coordinates. The colors show the gas density (top left), radiation energy density (2nd panel, left), gas temperature (3rd panel, left), magnetic field strength (bottom left), gas lorentz factor γ (top right), gas magnetization σ (2nd panel right), gas pressure to magnetic pressure ratio $p_{\rm gas}/p_{\rm mag}$ (3rd panel, right), and gas to radiation pressure ratio $p_{\rm gas}/p_{\rm rad}$ (bottom right).

illustrate that the simulations show an increase in Poynting flux in the jet as the spin increases. The high velocity component with $\gamma > 2$ is likely due to Poynting acceleration, which is more efficient in more magnetized jets (Chatterjee et al. 2019). Also of note is the fact that the funnel is optically thin down to $r \approx r_H$ near the poles (Fig. 6), which suggests radiative acceleration will be weak near the poles and cannot accelerate the $\gamma > 2$ component. In addition, the trend of increasing jet velocity as spin increases was demonstrated in GRMHD SANE models by Penna, Narayan & Sądowski (2013).

Although we performed similar simulations in Curd & Narayan (2019) but with $M_{\rm BH} = 10^6\,{\rm M}_\odot$, the SANE $a_* = 0.9$ model in that work (model `s09`) did not produce a relativistic jet (Curd & Narayan 2019, figure C5), contrary to the models with $a_* \geq 0.5$ in this work. The results for the outflow in `s09` were assumed to be robust since the angular resolution of $N_\vartheta = 320$ is large compared to many previous simulations in the literature. For instance, SANE models presented by Penna et al. (2013) launched a relativistic jet with only $N_\vartheta = 128$. As we demonstrate in Appendix A, it is necessary to employ

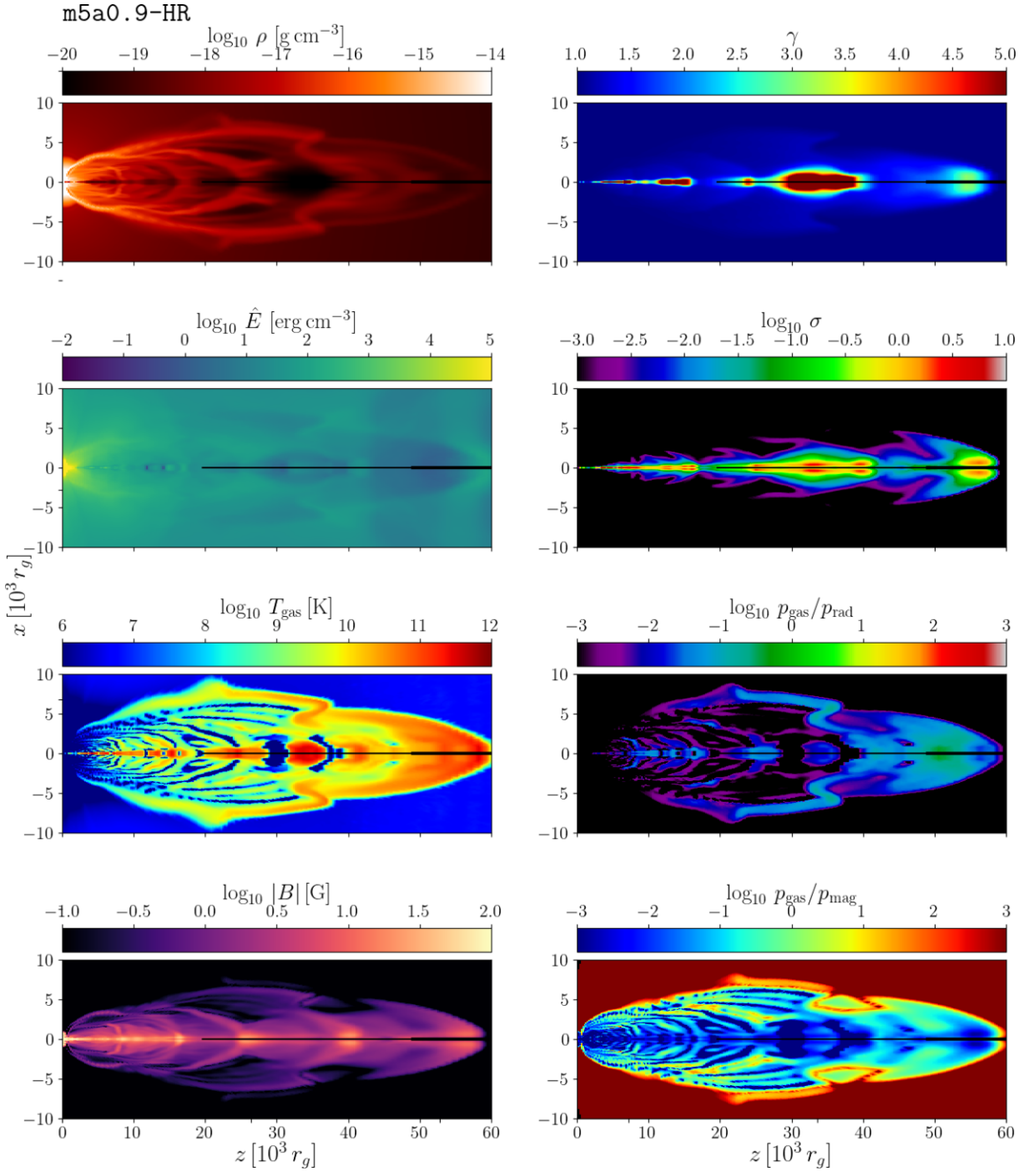

Figure 9. The same as Fig. 8, but for model `m5a0.9-HR` at $t = 83\,000\,t_g$. Note that we have increased the range of λ to highlight the maximum jet velocity. The simple addition of a spinning BH has a noticeable effect in many characteristics of the jet. Namely, the jet propagates farther owing to a high velocity component near the poles with $\gamma > 2$. In addition, the jet is hotter along the jet axis and jet head. Lastly, the magnetic field strength in the jet is larger at larger radii ($r > 30\,000\,r_g$), which leads to more of the gas becoming strongly magnetized with $\sigma > 1$. Regions where the jet pinches towards the polar axis (i.e. at $z \approx 25\,000\,r_g$) signifies recollimation shocks are also present.

adequate resolution in the polar region for the jet launching and structure to be captured. This is possibly due to the large-scale initial torus that we employ since the flow properties can be effected by the scale of the initial torus as was illustrated by Chatterjee et al. (2019).

The increased jet power and magnetization in the jet as the BH spin increases suggests the Blandford–Znajek mechanism is a driving factor. Although the total jet efficiency will be very weak ($\lesssim$1 per cent) assuming the magnetic flux and BH spin values in Table 1. Given the appearance of a relativistic jet in our models, which are a more conservative assumption for the accretion disc state than a MAD scenario, one wonders why the vast majority of TDEs appear to not have a jet and if the SANE scenario can still apply to non-jetted TDEs.

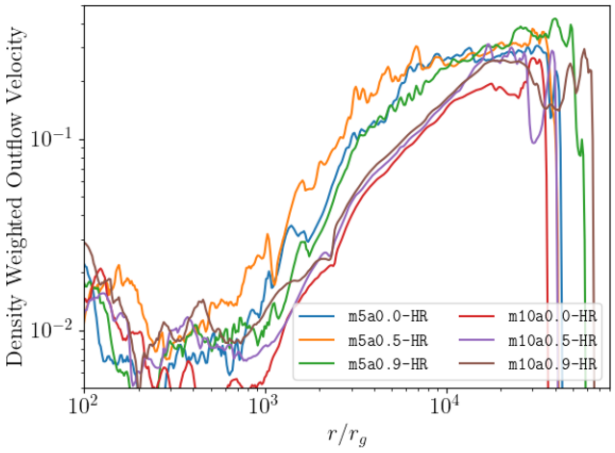

Figure 10. Here, we present radial profiles of the density weighted outflow velocity in the jet for each model at the final snapshot. The behaviour is similar in each model. The density weighted outflow velocity shows acceleration between $10^3 \lesssim r/r_g \lesssim 10^4$. Beyond $10^4\, r_g$, the velocity seems to have reached a plateau of ∼0.2–0.35c.

The fact that TDEs likely form misaligned discs provides a plausible explanation, especially in the case of weak jets, since a weak jet launched along the BH spin axis will have a hard time penetrating the surrounding TDE debris. In addition, the flux of poloidal magnetic field threading the BH, which is the result of our initial conditions and the magnetic dynamo that we employ, may be even lower than in our simulations. Assuming a purely Blandford–Znajek powered jet, even a magnetic flux of unity would reduce the jet power by more than factor of 10.

Since the accretion rate is only marginally super-Eddington, radiation can more efficiently escape and the radiative efficiency $\eta_{\rm rad}$ is only a few per cent smaller than the Novikov-Thorne (NT) efficiency as a result. The accretion flow generates a jet and wind with a total energy flux that is a fraction of the accretion power. We find $(\eta_{\rm wind} + \eta_{\rm jet}) \approx 0.6 - 3.6$ per cent. We also observe a clear trend of increasing energy outflowing in the jet and wind as the spin increases for a given BH mass, reflecting the overall increase in energy extracted from the system ($\eta_{\rm tot}$) as the BH spin increases.

Although the jet power increases and the jet near the polar axis becomes significantly more relativistic as the spin increases, the density weighted outflow velocity is surprisingly similar across BH mass and spin. As we show in Fig. 10, each model only achieves an outflow velocity of ∼0.2–0.35c in a density weighted sense. The acceleration of the gas between $10^3 \lesssim r/r_g \lesssim 10^4$ is also clearly illustrated. This is in agreement with the terminal density weighted jet velocity of ≈0.3c reported by Sądowski & Narayan (2015a), but we have demonstrated that the spin and jet magnetization does not appear to play a role in the velocity of the higher density component of the jet in SANE, super-Eddington accretion discs with $\dot{M} \gtrsim 11\dot{M}_{\rm Edd}$.

To search for dissipation in the jet, we examine the gas entropy per unit mass:

$$s_{\rm gas} = \frac{1}{\gamma_g - 1} \ln\left(\frac{p_{\rm gas}}{\rho^{\gamma_g}}\right), \tag{37}$$

and the log scaled radiation entropy per unit mass:

$$s_{\rm rad} = \log_{10}\left(\frac{4aT^3}{3\rho}\right). \tag{38}$$

The variable velocity of gas flowing along the jet is expected to lead to shocks, wherein dissipated kinetic energy leads to heating of the gas and thus an increase in internal energy. In addition, we observe multiple recollimation features, which are also sites of shocks and dissipation, along the jet axis which appear more significant in the models with $a_* > 0$ (see the top-left panel in Fig. 9 for instance). Recollimation features have been seen in various numerical studies of jets (Kohler, Begelman & Beckwith 2012; Lazzati et al. 2012; Mizuno et al. 2015; Bromberg & Tchekhovskoy 2016; Hervet et al. 2017), and it has been demonstrated that recollimation shocks appear due to a pressure mismatch between the jet and the surrounding medium. We consider the radial velocity, gas entropy, and radiation entropy in `m5a0.5-HR` in Fig. 11. The trace of the entropy in both gas and radiation at $\vartheta \approx 3^\circ$ shows quite clearly that (i) a strong shock exists at the jet head, (ii) internal shocks are present within the jet, (iii) the entropy shows similar oscillations to the velocity, and (iv) the entropy generally increases between $z \sim 5000 - 40\,000\, r_g$. Taken together, this suggests that the jet head is where dissipation is largest and we are indeed observing dissipation of kinetic energy via internal shocks within the jet at radii smaller than the jet head.

4.2 Jet structure

We define the jet boundary using the Bernoulli parameter via equation (19) and measure the half-opening angle $\vartheta_{\rm jet}$ for both the top and bottom jet as a function of distance along the jet (z, see Fig. 12). We find nearly identical opening angles for both the top and bottom jet in each model. We find that at distances $r_H/r_g < z/r_g \lesssim 1000$ the jet undergoes very nearly parabolic expansion with a power law of roughly $\omega \propto z^{0.7}$, where ω is jet width. The jet appears to maintain a roughly conical structure at jet lengths $1000 \lesssim z/r_g \lesssim 30\,000$ with $\vartheta_{\rm jet}$ maintaining a nearly flat profile. For $z/r_g \gtrsim 40\,000$, the jet angle shrinks rapidly at the jet head.

An important caveat that we must point out is that the break between the parabolic and conical region is a byproduct of the choice of initial torus. In each model, the break occurs very close to the radial extent of the initial torus model (∼ $3000\, r_g$, see Table 1). This point marks the transition from higher density gas, which can provide lateral pressure support, to the substantially lower density atmosphere, which provides negligible pressure support in comparison.

Conically expanding jets were successfully applied to ASASSN-14li in the models of Pasham & van Velzen (2018), who modelled the radio synchrotron emission as a superposition of synchrotron-emitting regions in a conically expanding jet. Fig. 12 demonstrates that SANE super-Eddington discs produce conically expanding jets, at least with our chosen initial torus configuration. The half-opening angles that we find are all larger than the best-fitting models of Pasham & van Velzen (2018). We note that their model assumed a previously cleared funnel was present while we have assumed a low-density atmosphere, which does not provide substantial lateral confinement. Future work on TDE jets should explore the effects of the atmosphere and initial torus in greater detail.

5 SYNCHROTRON EMISSION IMAGING ANALYSIS

In Fig. 13, we compare the emissivity of synchrotron and bremsstrahlung processes in `m5a0.0-HR`. We compute the emissivities using functions defined in Sądowski et al. (2017) since these are the frequency-dependent functions currently used by KORAL. Note that the equations presented in Sądowski et al. (2017) describe a two temperature plasma while we assume a single temperature plasma with $T_{\rm i} = T_{\rm e} = T_{\rm gas}$ to compare the contributions of synchrotron and bremsstrahlung processes. We use the fitting function for the

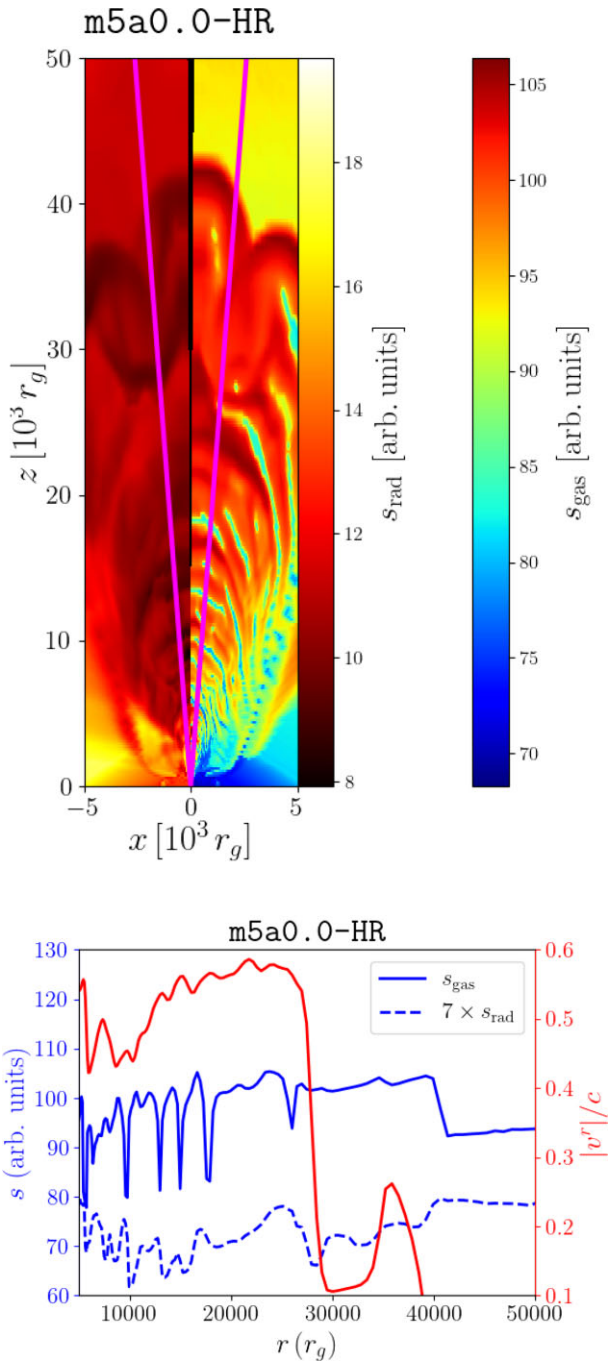

Figure 11. Here, we show the gas (right) and radiation (left) entropy in the top panel. The bottom panel shows a trace of the radial velocity (red) and both gas and radiation entropy (blue) taken at $\vartheta = 3^\circ$ (indicated as the pink line in the top panel). Dissipation leads to an increasing entropy in both gas and radiation overall. The sharpest jump occurs at the jet head ($z \approx 40\,000\,r_{\rm g}$). There are also several jumps in entropy down the jet axis (beginning at $r \lesssim 30\,000\,r_{\rm g}$ in this snapshot) which are internal shocks driven by fast moving gas shocking with slow moving gas within the jet. Similar features are seen in each simulation presented in this work.

ultrarelativistic synchrotron emissivity in Gaussian-CGS units:

$$j_{\rm Synch} = 4.43\times10^{-30}\nu_M n_e \frac{x_M I'(x_M)}{2\theta_e^2}\left[\frac{\rm erg}{\rm cm^3\,s\,Hz}\right], \quad (39)$$

where $n_{\rm e} \equiv \rho/(\mu m_p)$ is the electron number density in a fully ionized gas, given a mean molecular weight μ and proton mass $m_{\rm p}$, $\theta_e \equiv$

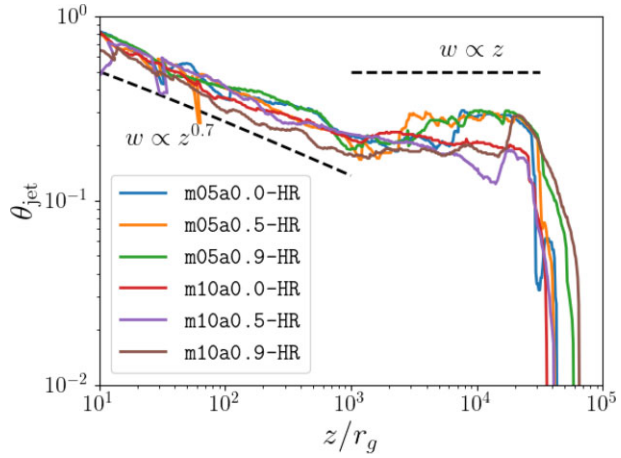

Figure 12. Here, we show the half opening angle of the jet (solid lines) for each model. Note that we have symmetrized the data by taking the mean of the half-opening angle measurement for the bottom and top jet. We find that the jet expands roughly conically from $z \approx 1000\,r_g$ until nearly $z \approx 40\,000\,r_{\rm g}$ in each model.

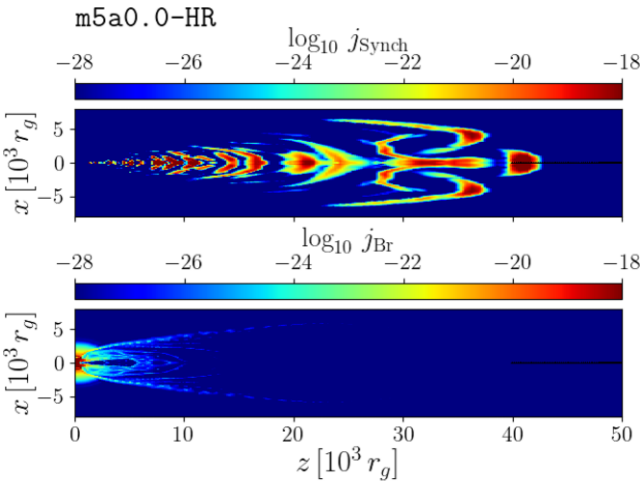

Figure 13. Here, we show the synchrotron emissivity (top panel) and the bremsstrahlung emissivity (bottom panel) at 1 GHz for `m5a0.0-HR`. We note that the spectra as presented in Sections 5.1 and 5.2 peak at >10 GHz; however, the choice to show the 1 GHz emissivities is to better visualize the spatial difference between bremsstrahlung and synchrotron emission in the jet. The synchrotron emissivity is dominant outside of the optically thick disc. The bremsstrahlung emissivity shown here is representative of the low frequency emissivity as the bremsstrahlung cutoff occurs at $\nu > 10^{16}$ Hz, far beyond the frequencies we consider in this work.

$kT_{\rm gas}/m_ec^2$ is the dimensionless electron temperature, $x_M = \nu/\nu_M$, $\nu_M = (3/2)eB\theta_e^2/2\pi m_e c$ is the characteristic synchrotron frequency, and $I'(x_M)$ is a fitting function provided by Mahadevan, Narayan & Yi (1996):

$$I'(x_M) = \frac{4.0505}{x_M^{1/6}}\left(1+\frac{0.40}{x_M^{1/4}}+\frac{0.5316}{x_M^{1/2}}\right)\exp(-1.8899x_M^{1/3}). \quad (40)$$

The bremsstrahlung emissivity is computed as:

$$j_{\rm Br} = \frac{6.8\times10^{-38}}{4\pi}T_{\rm gas}^{-1/2}n_e^2\bar{g}R(T_{\rm gas}) \times \exp(-h\nu/kT_{\rm gas})\left[\frac{\rm erg}{\rm cm^3\,s\,Hz}\right], \quad (41)$$

where we assume a Gaunt factor $\overline{g} = 1.2$ and $R(T_{\rm gas}) \equiv 1 + 4.4 \times 10^{-10}(T_{\rm gas}/1\,{\rm K})$ is a relativistic correction adopted from Rybicki & Lightman (1979). The frequency ν_M sets the peak of the synchrotron emission in this formulation.

We find that the synchrotron emission dominates the jet while bremsstrahlung dominates in the optically thick disc, thus we expect the jet emission will largely be from synchrotron processes. The periodic outflows appear as discrete 'bubbles' of high synchrotron emission along the jet. Here, the gas is hotter and high frequency synchrotron emission ($\nu \gtrsim 10^{11}$) is expected as a result. We note, however, that these computations were done directly from the KORAL data and do not represent the spatial intensity information as we have not accounted for opacity effects, viewing angle, and resolution, all of which may change which features can be observed. Nevertheless, this analysis demonstrates that the jet emission is not continuous. The previous description is true of each model considered in this work.

We also estimate the Compton-y parameter ($y = \tau_{\rm es} k T_{\rm gas}/m_{\rm e}c^2$, Rybicki & Lightman 1979) in the extended jet to test whether Compton effects are important. We find that $y \ll 1$ throughout the bulk of the jet, so Compton effects will also be minimal due to the low opacity. As such, the synchrotron emission alone can provide a reasonable model of the jet emission.

We make use of the GRRT code `ipole` (Mościbrodzka & Gammie 2018) to produce images of the jet that include ray-tracing and radiative transfer effects. Before post-processing the data, we set the gas density to zero, $\rho = 0$, in regions where $\sigma > 1$. GRMHD codes inject mass and energy in these regions to keep the simulation stable. As such, the accuracy of the radiation field from these regions is less certain than where $\sigma < 1$. This method, which is the most conservative choice, has been employed in other studies of ray-traced GRMHD simulations (Chael, Narayan & Johnson 2019). Because `ipole` does not presently include bremsstrahlung or Compton effects, we also cut out data for $r < 5000\,r_{\rm g}$ prior to ray-tracing.

5.1 Time evolution and viewing angle dependence of emission for $T_{\rm e} = T_{\rm i}$

We present viewing angle-dependent spectra for the $M_{\rm BH} = 5 \times 10^6\,{\rm M}_\odot$ models computed over $\nu = 10^9 - 10^{12}$ Hz for snapshots ranging from $t = 28\,000$ to $78\,000\,t_{\rm g}$ in Fig. 14. Here, we assume a single-temperature gas with $T_{\rm e} = T_{\rm i} = T_{\rm gas}$, where $T_{\rm gas}$ is taken directly from the KORAL simulation.

Focusing on the spectrum over time for each BH spin, we find that the jet is generally brightening across all frequencies. The emission becomes significantly brighter as the spin increases, reflecting the substantial increase in jet power as the spin increases (see Table 1). We observe weak beaming comparing the 10° and 90° spectra, as indicated by the shift to the left of each spectrum as the viewing angle increases.

For the $M_{\rm BH} = 10^7\,{\rm M}_\odot$ models (Fig. 15), we again observe only weak beaming and the jet becomes brighter as the BH spin increases, but there are several notable differences. First, the jet in `m10a0.0-HR` and `m10a0.5-HR` is actually dimming over time. For instance, at $t = 28\,000\,t_{\rm g}$, the jet in `m10a0.0-HR` has a peak luminosity of $\sim 5 \times 10^{39}$ erg s^{-1} and a peak frequency near 700 GHz, but by $t = 78\,000\,t_{\rm g}$ the jet has become less bright with a peak luminosity of $\sim 5 \times 10^{38}$ erg s^{-1} and a peak frequency near 100 GHz. The jet in `m10a0.9-HR`, on the other hand, is still brightening by the time we stop the simulation.

We note that the behaviour of `m5a0.0-HR` is atypical amongst the simulations presented in this work in that the jet first brightens, dims, and then rebrightens before the end of the simulation. After quickly brightening following the onset of accretion, the jet initially becomes less luminous and the peak frequency decreases until it reaches only ∼40 Hz at $t = 58\,000 t_{\rm g}$. For $t \lesssim 58,000\,t_g$, the jet emission is dominated by material near the head of the jet and not very much emission is present within the jet itself. As material at the jet head expands and cools, the brightness declines and the spectrum shifts to lower frequencies overall.

However, at $\sim 40\,000\,t_{\rm g}$, a high velocity (density weighted velocity of $\sim 0.1c$) component appears at the base of the jet, passing through the slower moving outflow and decelerating as it dissipates its kinetic energy. By $\sim 68\,000\,t_{\rm g}$, this component has caught up to material downstream and drives internal shocks within the jet between $z \sim 5000$ and $20\,000\,r_{\rm g}$. These shocks cause a significant amount of heating, driving the gas temperature where shocks occur to increase from $\sim 10^9$ to $\sim 10^{10}$ K. The internal shocks lead to high frequency emission, which is substantially brighter than that from the jet head alone. For instance, by $t = 78\,000\,t_{\rm g}$, the jet has brightened to a luminosity of nearly 5×10^{39} erg s^{-1} at the peak frequency versus the initial $\sim 10^{38}$ erg s^{-1} at $t = 28\,000\,t_{\rm g}$. This demonstrates clearly how significant the contribution of emission due to internal shocks is in the context of these models.

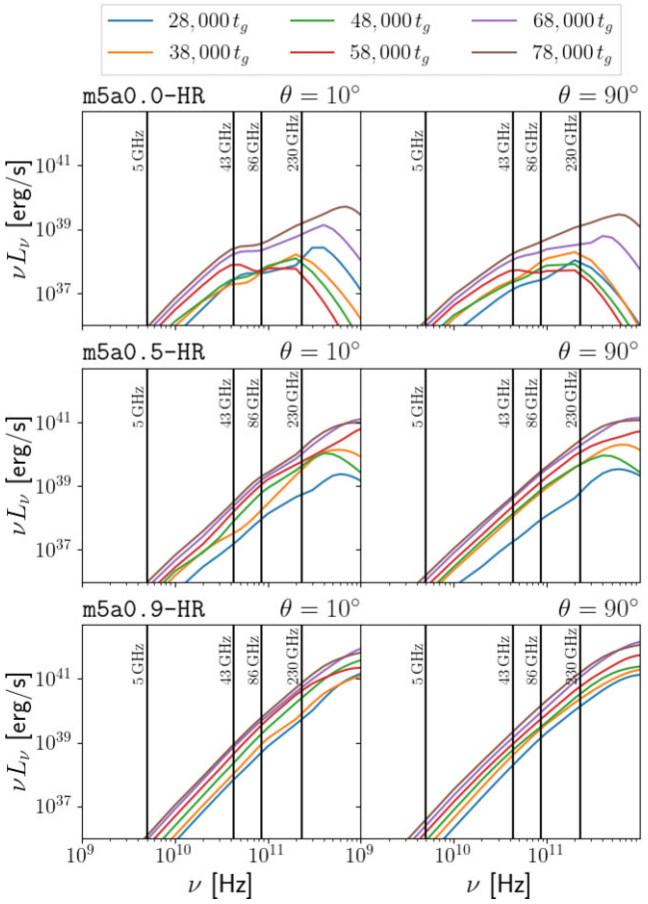

Figure 14. Here, we show spectra for `m5a0.0-HR` (top), `m5a0.5-HR` (middle), and `m5a0.9-HR` (bottom) computed for viewing angles of 10° (left) and 90° (right) at snapshots ranging from $t = 28\,000$ to $78\,000\,t_{\rm g}$. In each case, the jet is generally brightening across all frequencies; however, the jet becomes more energetic and the peak frequency becomes larger as the spin increases.

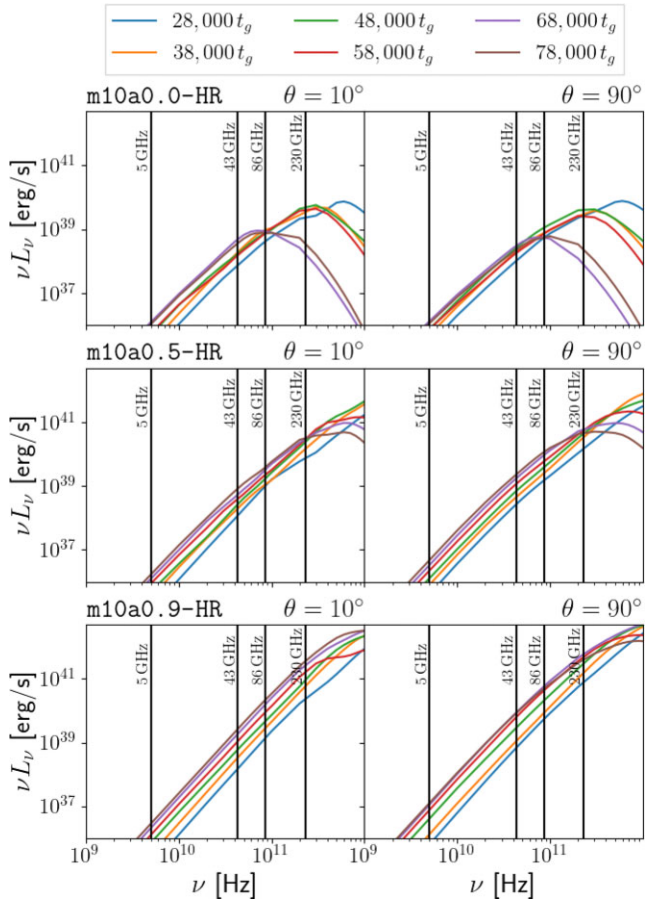

Figure 15. The same as Fig. 14 but for models `m10a0.0-HR` (top), `m10a0.5-HR` (middle), and `m10a0.9-HR` (bottom). In all cases, the spectrum is generally shifting to the left and the peak frequency also decreases as the jet expands and some of the gas cools. However, `m10a0.0-HR` begins to dim substantially and the 230 GHz luminosity drops from $\sim 5 \times 10^{39}$ erg s^{-1} at $t \leq 58\,000\,t_g$ to $\sim 10^{38}$ erg s^{-1} after $t = 68\,000\,t_g$. Model `m10a0.9-HR`, on the other hand, is still brightening at 230 GHz by the final snapshot.

With the exception of `m5a0.0-HR` and `m10a0.0-HR`, the difference between the $M_{\rm BH} = 5 \times 10^6\,{\rm M}_\odot$ and $M_{\rm BH} = 10^7\,{\rm M}_\odot$ models at late times ($t \gtrsim 58\,000\,t_g$) is in part because the jets have propagated a shorter physical distance due to the shorter time in physical units. Although each model was run $81\,200 - 83\,000\,t_g$ this only corresponds to ∼24 d for $M_{\rm BH} = 5 \times 10^6\,{\rm M}_\odot$ and ∼48 d for $M_{\rm BH} = 10^7\,{\rm M}_\odot$. Consequently, the jets for $5 \times 10^6\,{\rm M}_\odot$ have propagated roughly half the distance of the jets for $M_{\rm BH} = 10^7\,{\rm M}_\odot$. The jets for the $M_{\rm BH} = 5 \times 10^6\,{\rm M}_\odot$ models may also show dimming given a longer run time; however, `m5a0.0-HR` suggests that rebrightening events can also occur.

It is interesting to note the evolution of `m10a0.0-HR`, which is only bright at 230 GHz until $t = 58\,000\,t_g$. This suggests that high frequency radio/submillimetre emission (i.e. $\nu > 100$ GHz) from TDE jets may only last for several weeks depending on the BH spin. However, we have not taken into account the effects of varying the external medium nor the possible misalignment between the BH spin and accretion disc in this work. These two factors will have a non-negligible effect on the jet power and the jet evolution. Future studies should explore these factors to better understand TDE jets.

5.2 Effects of two-temperature plasma

Internal shocks in the jet are expected to produce non-thermal electrons, which we do not model in this analysis. In addition, these shocks are expected to lead to differential heating of electrons and ions. The plasma will retain memory of this because electrons and ions and cannot efficiently thermalize in low-density plasmas. This effect has been treated in studies of hot accretion flows using a simple two-temperature prescription. For instance, it is common to define an electron temperature that depends on β_g to differentiate the electron temperature in the jet and disc separately (Mościbrodzka, Falcke & Shiokawa 2016). Since we only model the jet emission, we adopt a simple approach and define the electron temperature via:

$$\frac{T_{\rm i}}{T_{\rm e}} = \mathcal{R}, \tag{42}$$

where $T_{\rm i}$ is set to $T_{\rm gas}$ from the KORAL simulation. This simplified prescription smooths over the microphysics, which depend on magnetic reconnection and shock properties; however, it does provide some handle on how the electron and ion populations must differ within a particular model to produce a specific emission property, albeit in a parametrized fashion. A recent study of electron heating in jets in active galactic nuclei (Ohmura et al. 2019, 2020) has demonstrated that $T_{\rm i}/T_{\rm e}$ can become as large as 10–100 depending on the heating physics. In these simulations, shocks led to ion heating while weak Coulomb coupling prevented the ion and electron populations from equilibrating. Our simulation results indicate that internal shocks due to variable ejections and recollimation take place. Furthermore, the time between Coulomb collisions is $>10^5$ yr for typical densities and temperatures in the jet, thus it is reasonable to model the electrons in the jet with $T_{\rm i}/T_e > 1$.

We present full spectra at selected times for each model in Fig. 16. In all models, we find that increasing $\mathcal{R}$ decreases the peak frequency and overall luminosity. In model `m10a0.5-HR` at $t = 83\,000\,t_{\rm g}$ for instance, as $\mathcal{R}$ is varied from 1 to 20, the peak frequency shifts from ∼200 to ∼20 GHz and the luminosity declines by nearly four orders of magnitude from $\sim 10^{41}$ erg s^{-1} to $\sim 10^{37}$ erg s^{-1}. As models `m5a0.0-HR`, `m10a0.0-HR`, and `m10a0.5-HR` illustrate, the electron temperature is extremely important for the high frequency emission as each of these models show greatly diminished emission at 230 GHz for $\mathcal{R} > 2 - 5$. For models `m5a0.5-HR`, `m5a0.0-HR`, and `m10a0.5-HR`, the jet luminosity at $\nu \gtrsim 230$ GHz is not as strongly diminished as $\mathcal{R}$ increases and $\mathcal{R} > 20$ is required to drop the peak frequency below 230 GHz. We explore the effects of $\mathcal{R}$ on the detectability of these models in the following section.

Studies of electron and ion heating suggest that the electron temperature might depend on β_g (e.g. Howes 2010; Rowan, Sironi & Narayan 2017), which would introduce spatial variation in $\mathcal{R}$. This would significantly change the behaviour in the spectra if regions that emit the most also have large values of $\mathcal{R}$. Without a heating prescription implemented during the simulation, however, we do not think it is justified to use a model which varies with β_g. That being said, a more accurate prescription may also need to account for the radiation pressure and use a two-temperature model which scales based on β_t. We leave a precise analysis of the spatial electron temperature ratio to a future analysis.

5.3 230 GHz images

In this section, we analyse viewing angle-dependent thermal synchrotron images at 230 GHz, which were calculated assuming $T_{\rm e} = T_{\rm i}$ and employ the same methods as in Section 5.1. In addition, we

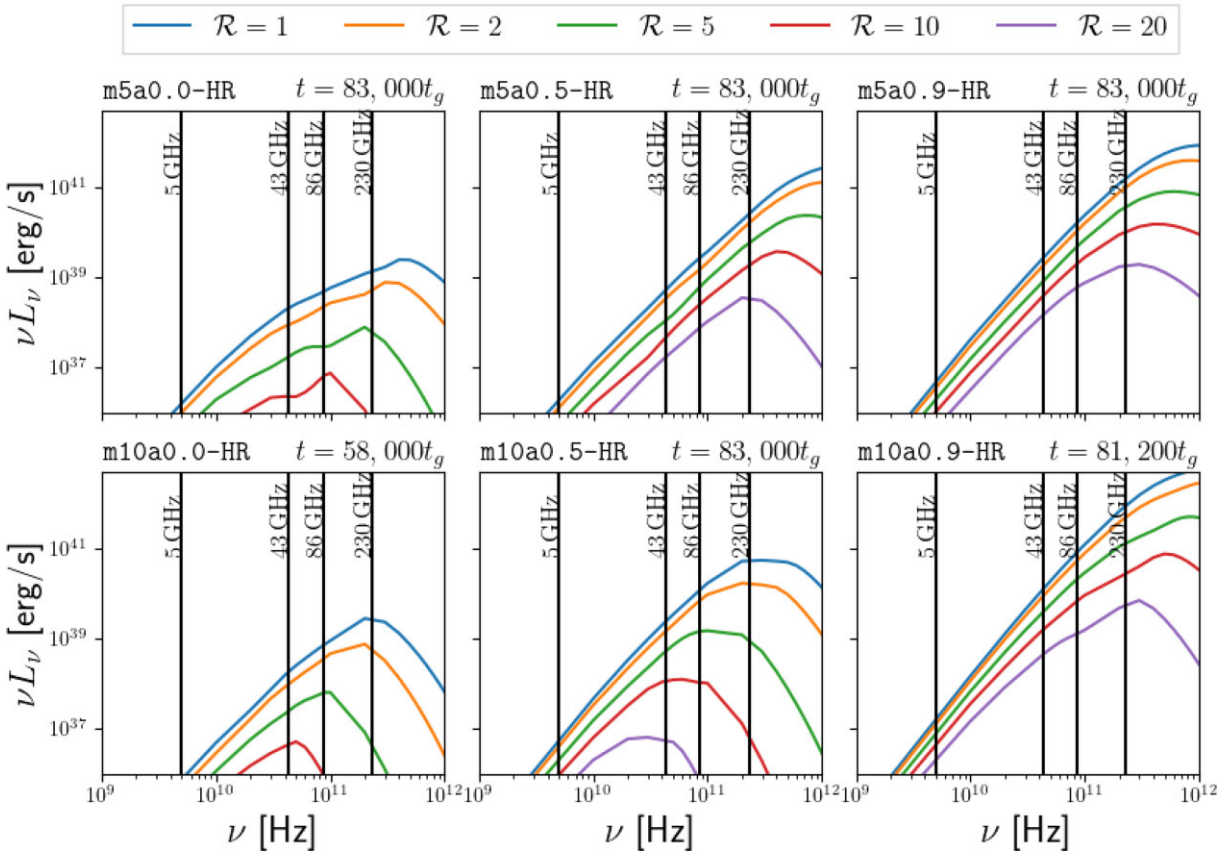

Figure 16. Here, we present model spectra of each model produced by varying $T_i/T_e = \mathcal{R}$. Here, we use a camera angle of $\theta = 90°$ (viewing the disc/jet edge on). Increasing $\mathcal{R}$ has the effect of decreasing both the peak frequency and luminosity in each model. Even a modest temperature ratio of $\mathcal{R} = 5$ can diminish the jet luminosity by 1–2 orders of magnitude. A temperature ratio of $\mathcal{R} \geq 5$ may also substantially diminish the 230 GHz flux for colder jets which has important consequences for detecting and resolving potential sources.

apply a Gaussian smoothing function with an FWHM of ΔR to each model to simulate the effects of the resolved angular scale ($\Delta\theta$) and distance to the source (D). The resolved scale in r_g can be related to both quantities by:

$$\frac{\Delta R}{r_g} \approx 2022 \left(\frac{M_{\rm BH}}{10^6\,{\rm M}_\odot}\right)^{-1} \left(\frac{D}{1\,{\rm Mpc}}\right) \left(\frac{\Delta\theta}{20\mu{\rm as}}\right). \quad (43)$$

For a given resolution scale, the image could represent a jet that is both distant and well resolved or nearby and poorly resolved. We blur each image with a Gaussian using $\Delta R/r_g = (10\,000, 25\,000, 50\,000)$. We first focus on `m10a0.9-HR` to describe key emission features as it is the brightest model with the largest physical scale.

In Fig. 17, we show the time evolution of the jet emission for a viewing angle of 90° in the left-most column. The jet in this model is extremely bright with $T_b > 10^{10}$ K. The jet emission is primarily from the jet head but there is also significant emission along the jet axis, where relativistic magnetized gas resides. Discrete features within the jet due to internal shocks, which are spatially separated, are also apparent in the emission features. In the next three columns, we apply a Gaussian smoothing function of size $\Delta R/r_g = 10\,000$, 25 000, and 50 000, respectively. Even for the resolution scale $\Delta R/r_g = 25\,000$, the jet is incredibly bright with $T_b > 10^9$ K and the motion of the expanding jet head could be tracked if the source were resolved with $\Delta R \lesssim 25\,000\,r_g$. Tracking the jet position may allow for the jet velocity to be constrained with a method independent of emission model assumptions.

In Fig. 18, we show the viewing angle dependence of the jet emission in `m10a0.9-HR` for a viewing angle of 10° (top row), 45° (middle row), and 90° (bottom row). The distinguishing features of the jet (the jet head and discrete internal shock emission) cannot be distinguished at 45° even with $\Delta R/r_g = 10\,000$. At 10°, the jet appears as a double lobed structure due to the top and bottom jet, but this would be seen as a compact source unless the jet is well resolved.

Additional 230 GHz images of the jets of each model near the brightest point in their evolution for a viewing angle of 90° are shown in Fig. B3. In general, the jets become brighter as the spin increases owing to the greater overall jet power. In addition, the jet head and internal shocks are also apparent for fairly well-resolved jets viewed edge on for models with $M_{\rm BH} = 5 \times 10^6\,{\rm M}_\odot$.

In Fig. 19, we illustrate the dimming in `m10a0.0-HR`. The emission in this model was dominated by the jet head with only weak internal shocks. As a result, the jet appears as simply two lobes separated spatially. As the jet head expands and cools, the high frequency emission declines rapidly as described in Section 5.1. If detected as a radio/submillimetre source, `m10a0.0-HR` would appear as a bright radio/submillimetre source for several weeks before likely dropping below detection limits.

On the other hand, the model `m5a0.0-HR` (Fig. 20) initially did not show internal shocks and was incredibly dim. Instead, the jet would have likely appeared to be dormant for several weeks before brightening if this model were observed immediately following the launch of the outflow. Although the time-scale before the jet brightens (∼20 d) is shorter than the delays seen in many radio-quiet TDEs

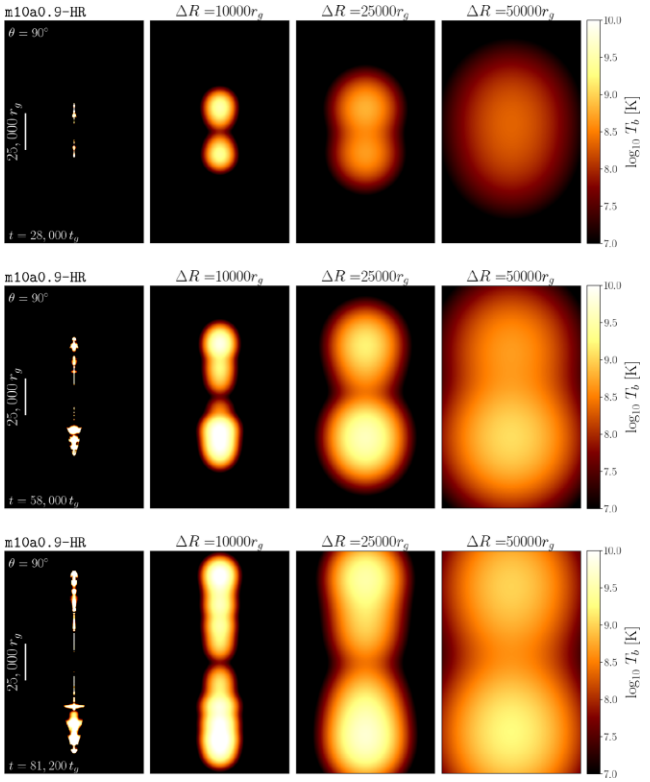

Figure 17. Here, we present GRRT images of the thermal synchrotron emission (mapped via the brightness temperature T_b) at $\nu = 230$ GHz with a viewing angle of $\theta = 90°$ for model `m10a0.9-HR`. Here, we have simply assumed $T_e = T_i$. We plot a white line of length $25\,000\, r_g$ in the left column for scale. We show snapshots at $28\,000\, t_g$ (top row), $58\,000\, t_g$ (middle row), and $81\,200\, t_g$ (bottom row). We show the infinite resolution images in the first column from the left. In addition, we apply Gaussian smoothing with a FWHM of $\Delta R/r_g = 10\,000$ (second column from the left), 25 000 (third column from the left), and 50 000 (right column) to illustrate the effects of blurring due to distance and resolution. The jet head is the brightest feature and in the infinitely resolved case appears to show bow shock features. For well-resolved images, bright 'bubbles' along the jet axis can be seen, similar to what we presented in the emissivity maps in Fig. 13. The jet head features are best resolved when $\Delta R \lesssim 25\,000\, r_g$. Observations with similar resolution scales may allow for direct measurement of the ejecta velocity.

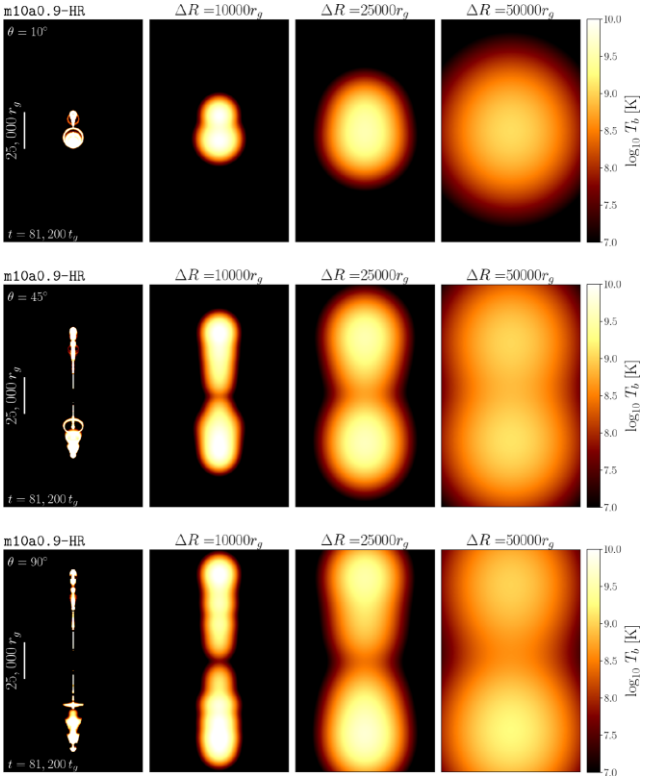

Figure 18. Similar to Fig. 17, but here each row shows `m10a0.9-HR` at $t = 81\,200\, t_g$ but with a viewing angle of $\theta = 10°$ (top row), $\theta = 45°$ (middle row), and $\theta = 90°$ (bottom row). The images at $\theta = 45°$ illustrate that internal shock features cannot be distinguished even for fairly well-resolved sources as the viewing angle decreases from edge-on. For jets viewed nearly down the axis (top row), only the jet heads are seen and the jet appears as two blurred lobes. For poorly resolved sources, a nearly face-on jet begins to look like a compact source.

(>30 d; Alexander et al. 2020) and we are imaging in a higher frequency than the 5–8.4 GHz most detections have been made at, this behaviour shows that delayed brightening can occur in super-Eddington accretion disc jets.

To estimate the viability of detection and resolution of each model, we estimate the visibility amplitude as a function of baseline distance assuming a detector limit of $\sigma_{230\,\mathrm{GHz}} = 10$ mJy for the EHT (Event Horizon Telescope Collaboration 2019) and $\sigma_{230\,\mathrm{GHz}} = 5$ mJy for the ngEHT (Doeleman et al. 2019) and assuming that Earth baselines at 230 GHz will not exceed 10 Gλ. Visibility amplitudes were calculated using the `eht-imaging` library (Chael et al. 2018). We consider a jet model detectable and resolvable if (i) the total image (zero fringe spacing baseline) flux is above $5\sigma_{230\,\mathrm{GHz}}$, (ii) the difference between the total image flux and any other, longer baseline (up to 10 Gλ) flux is above $5\sigma_{230\,\mathrm{GHz}}$, and (iii) the nominal resolution of the baseline ($1/u$ for baseline length u) is less than ΔR. This definition assumes that the baseline length is the maximum baseline separation available for the observations. Given this assumption, it additionally requires that the baseline can resolve the jet at the desired length scale. We

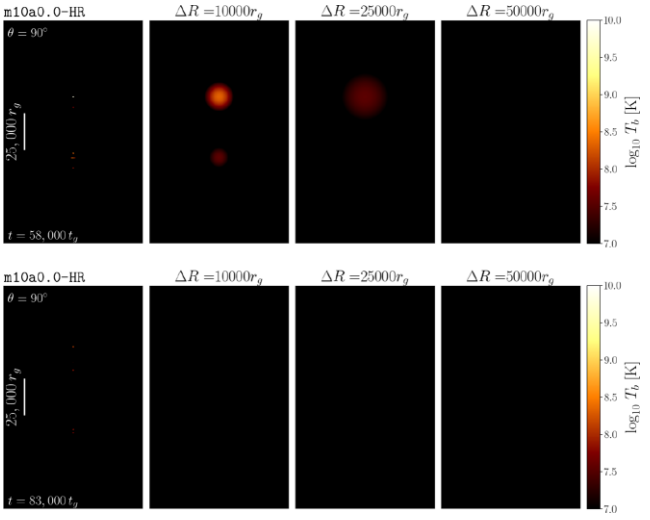

Figure 19. Similar to Fig. 18, but here we show `m10a0.0-HR` at $t = 58\,000\, t_g$ (top row) and $t = 83\,000\, t_g$ (bottom row) to illustrate the dimming of the jet. The jet in `m10a0.0-HR` did not show significant internal shock heating and as a result the jet head is responsible for most of the emission. As the jet head expands and cools, it eventually becomes dim, and possibly undetectable.

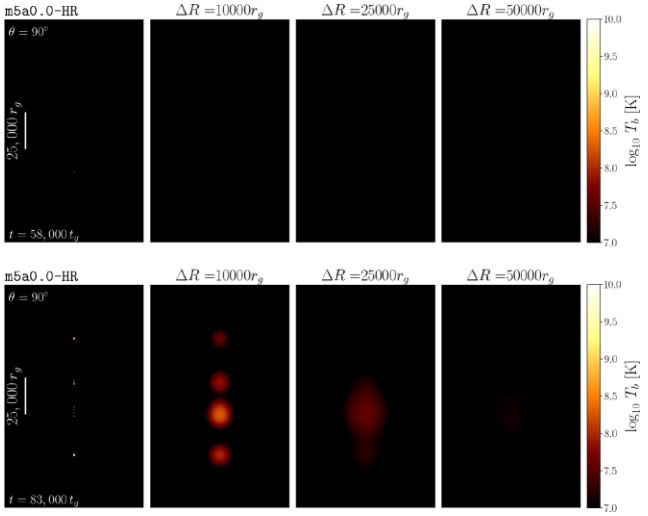

Figure 20. Similar to Fig. 19, but here we show `m5a0.0-HR` at $t = 58\,000\,t_g$ (top row) and $t = 83\,000\,t_g$ (bottom row) to illustrate the dimming of the jet. Similar to `m10a0.0-HR`, `m5a0.0-HR` also did not initially show significant internal shock heating but the initial jet was also quite weak and not significantly bright. By $t = 68\,000\,t_g$, the jet had brightened substantially due to internal shocks and shocks near the jet head where fast moving gas caught the slower moving jet head and energized it.

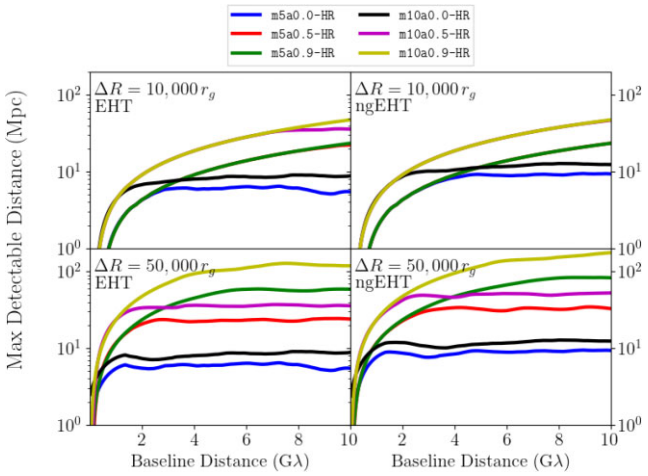

Figure 21. Here, we show the maximum distance at which the jet in each model is detectable and resolved given a limiting baseline distance and a $5\sigma_{230\,\mathrm{GHz}}$ (with $\sigma_{230\,\mathrm{GHz}} = 10$ mJy for the EHT and $\sigma_{230\,\mathrm{GHz}} = 5$ mJy for the ngEHT) detection threshold. It is assumed that $T_e = T_i$ ($\mathcal{R} = 1$). Note that in the top panels, the curves for `m5a0.5-HR` and `m5a0.9-HR` (as well as `m10a0.5-HR` and `m10a0.9-HR`) largely coincide since the maximum distance is resolution limited instead of flux limited as the baseline distance increases. Focusing first on the results assuming observations with the EHT (left), the estimated maximum distance at which each model can be detected increases with BH spin due to the increase in jet power and brightness. The non-spinning models require $D \lesssim 6$–9 Mpc regardless of resolution scale and are thus unlikely targets. The spin $a_* = 0.5$ models are substantially brighter and may be suitable targets at up to $D \lesssim 35$ Mpc. In the brightest model (`m10a0.9-HR`), resolving the internal shocks ($\Delta R = 10\,000\,r_g$) requires that the TDE occur within $D \lesssim 45$ Mpc while resolving only the jet head ($\Delta R = 50\,000\,r_g$) only requires $D \lesssim 110$ Mpc. The increased detector sensitivity expected in the ngEHT (right) compared to the EHT (left) increases the maximum distance at which the jets can be detected and resolved by a factor of ∼1.4–1.8. The greatest improvement is for large baseline distances and $a_* = 0.9$. For instance, the maximum distance increases from ∼110 to ∼180 Mpc at a baseline distance of 10 Gλ.

compute the maximum distance for viewing angles of 10°, 45°, and 90° and then average over viewing angle to obtain a representative maximum distance. We also smooth the maximum distance profiles using a moving average with a window of ∼2.7 Gλ in order to reduce scatter introduced by the variable behaviour in the visibility amplitude.

We present the estimated maximum distance for imaging a resolved jet near the brightest period in each simulation assuming $\mathcal{R} = 1$ with $5\sigma_{230\,\mathrm{GHz}}$ significance at length-scales $\Delta R = 10\,000\,r_g$ and $\Delta R = 50\,000\,r_g$ in Fig. 21. As expected, we find that the maximum distance at which the jet can be detected and resolved increases with BH spin due to the increased jet power. Assuming only the jet head is resolved, the brightest jets may be detected with the EHT (ngEHT) at up to $D \sim 110$ (180) Mpc depending on the baseline coverage available. The non-spinning models, on the other hand, are only detectable within $D \lesssim 6$–9 (8–13) Mpc. Assuming a middling BH spin of $a_* = 0.5$, detection may be possible at $D \lesssim 35$ (60) Mpc. Resolving finer structure requires that the TDE occurs nearby. For instance, `m10a0.9-HR` is only detectable and resolved within $D \lesssim 45$ Mpc if $\Delta R = 10\,000\,r_g$. The same maximum distance is found for the ngEHT assuming a resolution length-scale of $\Delta R = 10\,000\,r_g$. A similar effect on the maximum distance is seen in the other models as the resolved length scale decreases.

We quantify the effects of a two-temperature plasma by determining the maximum detectable and resolved distance for each model as $\mathcal{R}$ is varied assuming a baseline separation of 10 Gλ and a length-scale $\Delta R = 50\,000\,r_g$ in Fig. 22. Due to the decline in overall luminosity and the shift in peak frequency, the maximum distance can decrease by up to an order of magnitude. For instance, the maximum distance for `m10a0.9-HR`, assuming EHT detector limits, declines from ∼110 Mpc for $\mathcal{R} = 1$ to ∼8 Mpc for $\mathcal{R} = 20$. In models `m5a0.0-HR`, `m10a0.0-HR`, and `m10a0.5-HR`, even a small increase in $\mathcal{R}$ shifts the peak frequency to less than 230 GHz, which leads to unresolved 230 GHz jet emission for values of $\mathcal{R} > 1 - 2$ (assuming a lower threshold on the distance to the TDE of 1 Mpc). A similar result is found assuming the expected detector sensitivity of ngEHT, but the maximum distance increases by a factor of ∼1.4–1.8. In some cases, the maximum temperature ratio $\mathcal{R}$ that the jet can have and still be detectable increases (i.e. model `m5a0.9-HR`).

Our results suggest that the number of sources that can be detected and resolved will depend on the spin distribution of SMBHs across cosmic distance due to the increase in jet power with BH spin. Current simulations and observations that have estimated the spins of BHs at redshift $z \approx 0$ indicate that SMBHs in the mass range of $\sim 10^{6.5} - 10^{7.5}\,\mathrm{M}_\odot$ will tend towards $a_* \sim 1$ (Dotti et al. 2013; Reynolds 2013; Dubois, Volonteri & Silk 2014; Bustamante & Springel 2019). This is encouraging since, with the EHT (ngEHT), at least ∼45 (200) TDEs are expected per year within $D \lesssim 110$ (180) Mpc assuming $\mathcal{R} = 1$. This suggests that the increased detector sensitivity expected in the ngEHT could increase the number of possible TDE targets by a factor of nearly 4 compared to the EHT. On the other hand, if $\mathcal{R}$ significantly exceeds unity, less than one resolvable source may occur per year, even with the improved sensitivity of the ngEHT. In addition, if accretion occurs in the MAD accretion state for a significant fraction of a BH's lifetime, this could skew the BH spin distribution towards lower spin values due to spin-down (Narayan et al. 2022) which would certainly reduce the number of detectable TDE jet sources at larger distances based on our models.

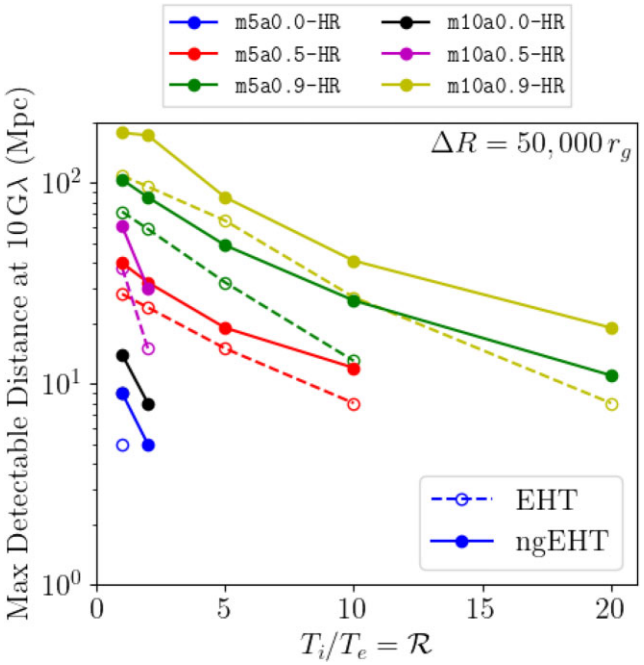

Figure 22. Here, we show the maximum distance at which the jet in each model is detectable and resolved as $\mathcal{R}$ increases for $\Delta R = 50\,000\, r_g$ at a limiting baseline distance of 10 Gλ. We compare EHT ($\sigma_{230\,\mathrm{GHz}} = 10$ mJy, dashed lines with open circles) and ngEHT ($\sigma_{230\,\mathrm{GHz}} = 5$ mJy, solid lines with filled circles) limits for the correlated flux density and a $5\sigma_{230\,\mathrm{GHz}}$ detection threshold. The curve is cut off at $\mathcal{R}$ where the jet becomes unresolved.

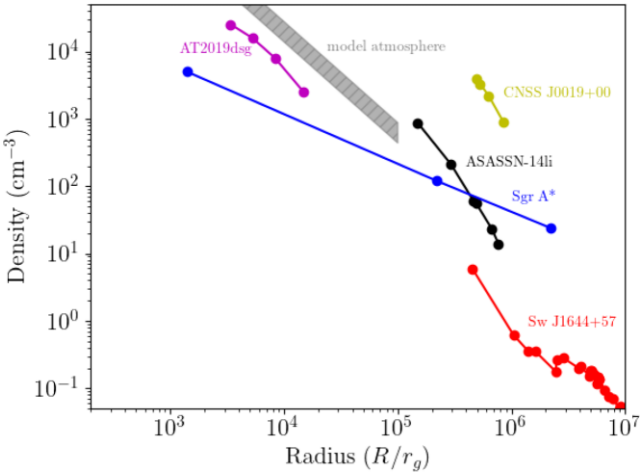

Figure 23. Here, we compare our model atmospheres (grey hatched region) with CNM profiles of ASASSN-14li (Alexander et al. 2016), CNSS J0019 + 00 (Anderson et al. 2020), *Swift* J1644+57 (Sw J1644 + 57, Eftekhari et al. 2018), AT2019dsg (Stein et al. 2021), and Sagittarius A∗ (Sgr A∗, Baganoff et al. 2003; Gillessen et al. 2019). The scaling in our models is such that the density of the CNM at large radii is similar to that inferred in other TDEs and Sgr A∗.

6 DISCUSSION

6.1 Initial atmosphere versus inferred profiles in TDEs

As noted in Section 3.3, we initialized each simulation with a low-density atmosphere where $\rho \approx (0.5 - 1 \times 10^{-14}\,\mathrm{g\,cm^{-3}})(\mathrm{r}/\mathrm{r}_0)^{-3/2}$, where $r_0 = r_H$. The $r^{-3/2}$ profile that we have chosen is shallower than the inferred profile of roughly $r^{-5/2}$ for ASASSN-14li (Alexander et al. 2016). We note, however, that estimates of the density profile of ASASSN-14li were only obtained up to $\gtrsim 10^5 r_g$ (or $\gtrsim 10^4\, r_g$ if the outflow geometry is conical). Assuming that such a profile does indeed continue to the BH, this implies that the atmosphere in ASASSN-14li may reach a density near the horizon of $\sim 10^{-11}\,\mathrm{g\,cm^{-3}}$, nearly three orders-of-magnitude denser than we have implemented. On the other hand, the profile of the TDE AT2019dsg (Stein et al. 2021) appears to be turning over to a shallower profile of nearly r^{-1} at $r \lesssim 10^3\, r_g$, which is similar to the inferred properties of the CNM in Sagittarius A* (Baganoff et al. 2003; Gillessen et al. 2019). Extrapolating the profile of AT2019dsg down to the horizon implies a maximum density of $\sim 10^{-17}\,\mathrm{g\,cm^{-3}}$, which is orders of magnitude less than what we have implemented.

Despite these differences in the behaviour at small radii, our model atmospheres are similar to that of previous radio TDEs over $r \sim 10^4 - 10^5\, r_g$ (see Fig. 23), the region over which we present our spectra and images. The density profiles of TDEs have only been estimated for a small handful of radio TDEs. As of yet, the behaviour of the density profile down to $r \sim 1000 r_g$ has only been measured in AT2019dsg, while the other known TDEs have profile measurements down to $r \gtrsim 10^4 r_g$. Additionally, the overall scale of the gas density (i.e. the value of $\rho_{\mathrm{atm,\,max}}$ as defined in Section 3.3) appears to vary between systems. For instance, the CNM in the radio TDE CNSS J0019 + 00 at $r \approx 10^6\, r_g$ has the same estimated density as ASASSN-14li at $r \approx 10^5\, r_g$. Simulations with more dense atmospheres should be explored, as well as more or less steep gas density profiles, as the jet may experience strong deceleration and/or collimation as it encounters the CNM (e.g. see Barniol Duran, Tchekhovskoy & Giannios 2017).

6.2 Comparison with radio TDEs

The density weighted outflow velocity of each model is ∼0.2–0.35c, which is mildly relativistic but substantially faster than the $\lesssim 0.1c$ found in most radio-quiet TDEs so the outflow properties cannot explain the inferred velocities in these transients. Of note, however, is the production of $\gamma > 2$ gas in the jet for the $a_* \geq 0.5$ models. Sądowski & Narayan (2015a) found that the isotropic equivalent luminosity for highly super-Eddington ($\dot{M} > 10^3 \dot{M}_{\mathrm{Edd}}$) accretion flows can exceed $10^{47}\,\mathrm{erg\,s^{-1}}$, which is sufficient to explain the $\sim 10^{48}\,\mathrm{erg\,s^{-1}}$ X-ray equivalent luminosity seen in *Swift* J1644 + 57 (Bloom et al. 2011; Burrows et al. 2011). However, they performed simulations with $a_* = 0$ models and suggested that a $\gamma \gtrsim 2$ component may be untenable with radiative acceleration. Our simulation results suggest that for mass accretion rates $\sim 11 - 25 \dot{M}_{\mathrm{Edd}}$ (compared to the $\sim 45 - 4800 \dot{M}_{\mathrm{Edd}}$ in Sądowski & Narayan 2015a), the Poynting flux may result in a relativistic component. Not only does the jet power increase substantially as the BH spin increases in our simulations, but a relativistic jet component with $\gamma > 2$ is produced. This is due to increased magnetic energy flux in the jet, which leads to Poynting acceleration of gas where $\sigma > 1$.

Assuming $T_{\mathrm{e}} = T_{\mathrm{i}}$, the thermal synchrotron spectra presented in this work suggest that super-Eddington accretion discs can produce highly energetic jets, which primarily emit at $\nu > 100$ GHz and are bright with $L \sim 10^{41}\,\mathrm{erg\,s^{-1}}$ for >48 d. This is in staunch contrast with the radio properties of non-jetted TDEs. Non-jetted TDEs all appear to have a peak frequency of the order $\nu_{\mathrm{peak}} \sim 10$ GHz and have a luminosity of $L_{\mathrm{radio}} \approx 10^{37} - 10^{39}\,\mathrm{erg\,s^{-1}}$ at the time of detection.

The jet emission models which are brightest at 230 GHz, and thus the most favourable for detection in terms of ngEHT observations, are $\mathcal{R} = 1$. However, these models are in conflict with TDE observations

in terms of the peak frequency. The thermal synchrotron models that peak at smaller frequencies, and are thus more similar to known radio TDEs in terms of the peak frequency at least, have $\mathcal{R} > 10$. Nevertheless, none of our models are able to remain bright enough ($L_{\rm radio} \gtrsim 10^{37}$ erg s^{-1}) and simultaneously peak at $\lesssim$10 GHz.

Another possibility is that jets in these models will continue evolving towards lower frequencies and luminosity and we are simply observing a higher energy stage of the jet. For example, the low-frequency luminosity in each of our models at $\nu \approx$ 5–8.4 GHz (where most radio TDEs have been observed) is dimmer than non-jetted TDEs. However, our models showed evolution towards lower frequencies, and in the case of `m10a0.0-HR`, the luminosity at the peak frequency is also decreasing over time. This suggests that our models may evolve towards spectra more similar to radio-quiet TDEs given enough time.

This is an observationally interesting possibility since the majority of follow-up observations of TDEs in the radio have been at 5–8.4 GHz. Our models have a luminosity of $\lesssim 10^{36}$ erg s^{-1} at 5–8.4 GHz, placing them below upper limits in the majority of TDEs where no radio emission was detected (mostly $> 10^{37}$ erg s^{-1}, see fig. 1 of Alexander et al. 2020). If there is indeed a radio/submillimetre component at $\nu > 100$ GHz that is bright for the first few weeks of non-jetted TDEs, low-frequency searches are likely to miss this emission. Our results suggest earlier follow-up observations at high frequencies may be necessary to capture the full radio/submillimetre activity of some TDEs.

7 CONCLUSIONS

We have analysed outflows from SANE super-Eddington accretion discs across mass and spin parameter space with mass accretion rates $\dot{M} \gtrsim 11\dot{M}_{\rm Edd}$. We confirm that dissipation takes place at the jet head as well as along the jet due to internal shocks. These internal shocks are due to variable ejections of high velocity gas, which propagate along the jet axis and shock with slower moving gas within the jet, as well as recollimation shocks. The jet power and maximum velocity of gas near the pole increases with BH spin and models with $a_* \geq 0.5$ launch $\gamma > 2$ gas that is low density. However, we find that the density weighted outflow velocity is roughly $\sim$0.2–0.35c for each model.

Through GRRT post-processing with `ipole`, we produce time-dependent thermal synchrotron spectra assuming a single temperature plasma. The spectra peak at >100 GHz in each model and the overall radio/submillimetre luminosity increases with BH spin. In general, the jet head brightens as it expands into the CNM. However, models `m10a0.0-HR` and `m10a0.5-HR` appear to be dimming as they evolve. In addition, model `m5a0.0-HR` shows a delayed jet brightening with its jet remaining initially dim with $L \sim 10^{38}$ erg s^{-1} and increasing to $L \sim 5 \times 10^{39}$ erg s^{-1} at $t > 58\,000\,t_{\rm g}$.

We also test a simple electron temperature model. We find that increasing $T_i/T_e = \mathcal{R}$ has the effect of reducing the peak frequency and the overall luminosity. For instance, we found that $\mathcal{R} = 20$ reduced the peak frequency from $\sim$200 to $\sim$20 GHz and the luminosity from $\sim 10^{41}$ erg s^{-1} to $\sim 10^{37}$ erg s^{-1} in model `m10a0.5-HR`. We assumed the temperature ratio was independent of $\beta_g = p_{\rm gas}/p_{\rm mag}$, but there may be spatial variation in $\mathcal{R}$. In addition, a more accurate prescription may require some accounting for the radiation pressure as well since our simulations are in GRRMHD.

The 230 GHz images show that the brightest feature in each jet is the jet head, which shocks on the CNM. Internal shocks also produce bright 'bubbles' of emission at smaller radii in the jet. For sources resolved on scales $\Delta R \lesssim 10\,000\,r_{\rm g}$, we predict that the jet head and the internal shocks can be distinguished so long as the jet is not viewed at steep viewing angles. At poorer resolution ($\Delta R \lesssim 50\,000 r_{\rm g}$), the jet head is the most distinguishable feature.

We tested the viability of detecting and resolving the jets in each model at 230 GHz assuming flux limits appropriate to the EHT (ngEHT). The spin $a_* = 0.9$ models are bright enough to resolve the jet head within $\lesssim$110 (180) Mpc if $\mathcal{R} = 1$. At this distance, $\sim$45 (200) TDEs are expected per year, which suggests that several TDEs could be potential targets for radio/submillimetre follow-up during future observing missions. Our calculations suggest that at most a factor of 4 increase in the number of TDE targets is possible if the detector sensitivity is improved to 5 mJy in the ngEHT. If the electrons are significantly cooler than the ions, the maximum distance where resolved jets may be detected is significantly reduced. For example, we find a maximum resolved distance of $\sim$8 (18) Mpc for $\mathcal{R} = 20$, which would reduce the number of potential targets per year to less than one even for the ngEHT. Our simulations may apply to the super-Eddington phase of a TDE, roughly $\sim 2t_{\rm fb}$ ($\approx$1 −several months). We suggest that high frequency radio/submillimetre follow-up of nearby TDEs during this early period be conducted to search for radio/submillimetre jets.

We must stress that much is unknown about jet launching in TDEs, thus while the number of TDEs increases with distance, only a fraction of these may ever appear in the radio/submillimetre. In this work, we have merely provided an analysis of a single mechanism by which radio/submillimetre emission can be produced, that is jets from SANE, super-Eddington accretion discs, which undergo conical expansion, and determine the viability of detection of such jets with the EHT/ngEHT. As of this writing, the majority of known radio TDEs appear to have produced their radio emission through sub-relativistic gas shocking with the CNM. However, if the accretion flow is indeed super-Eddington, some fraction of future radio TDEs may launch jets similar to those described in this work. Our model spectra were below detection limits at 5 8.4 GHz, where most radio follow-ups to date have been conducted, which suggests that such jets may have escaped detection previously. Radio/submillimetre follow-up of TDEs at >100 GHz may reveal a higher energy component associated with a bipolar jet produced by a super-Eddington accretion disc.

Before we conclude, we must point out several caveats in this work. First, our initial conditions assume that the TDE debris stream efficiently and rapidly circularizes into an accretion disc. This may only apply to a subset of TDEs. For instance, Shiokawa et al. (2015) found that circularization during disc formation was quite poor and the disc remained highly eccentric for several times the fallback time (see also Curd 2021; Andalman et al. 2022). The case for the existence of poorly circularized TDE discs existing is supported observationally as well (Wevers et al. 2022). Nevertheless, a recent long duration (>60 d in physical time), high-resolution radiative hydrodynamics simulation by Steinberg & Stone (2022) has demonstrated that efficient disc circularization is possible. They report disc circularization near the peak of the TDE emission (at nearly 40 d in the simulation) for the fiducial case of a 10^6 M$_\odot$ BH disrupting a 1 M$_\odot$ star on a parabolic orbit with $R_{\rm p} = R_{\rm t}$; ergo, a circularized accretion disc near the peak emission of the TDE may be expected in some cases. Bonnerot & Lu (2020) and Bonnerot et al. (2021) also demonstrate substantial circularization of the TDE debris in their work.

Our simulation results demonstrate that in super-Eddington accretion discs, the jet magnetization is an important factor since it can produce a relativistic component driven by Poynting acceleration. Simulations of TDE accretion disc formation have not yet demonstrated the presence of significant magnetic flux in the inner

accretion flow nor the onset of jet launching so the highly magnetized, bright jets produced in the $a_* \geq 0.5$ simulations are somewhat of an idealization given the assumed initial torus configuration.

As we are limited to studying 2D simulations due to computational limitations, the explicit assumption that the jet is axisymmetric does not allow 3D instabilities to arise. The jet may kink and twist due to various MHD instabilities as it propagates (e.g. Barniol Duran et al. 2017). The kink instability, in particular, may give rise to additional dissipation of magnetic energy into thermal energy within the jet.

The mass accretion rates that our models achieve is not precisely at the peak accretion rate. This will change the jet power and potentially the radio/submillimetre brightness since $L_{\rm net} \propto \dot{M}$ (Sądowski & Narayan 2015a). In other words, the spectra we provide here may under/over estimate the jet brightness by a factor of a few. This may increase/decrease the maximum resolvable distance in some models, but the overall finding that some nearby TDEs may produce jets, which are detectable and resolvable, is robust.

The choice to cut out the $\sigma > 1$ region of the jet before ray tracing is conservative and well motivated, but the effects on the ray traced images has not yet been well studied. Given that much of the emission in the brightest jets originates from near the poles, our spectra provide a lower limit on the luminosity of the jet. In addition, as we have emphasized throughout this section, jets with internal shocks are likely to produce a non-thermal electron population and may also consist of a two-temperature plasma. Neither of these were employed during the simulations, and they could modify the jet properties since radiation is dynamically important.

ACKNOWLEDGEMENTS

We thank Ben Prather and George Wong for their assistance with the `ipole` code in this work. We thank Angelo Ricarte, Dominic Pesce, and Lindy Blackburn for helpful comments and discussions. We also thank the anonymous EHT publication committee referee who provided useful feedback. Lastly, we thank the anonymous referee who provided useful comments and critiques which improved the quality and clarity of this work. This work was made possible thanks to the NSBP/SAO EHT Scholars program and was supported in part by NSF grant AST-1816420, and made use of computational support from NSF via XSEDE resources (grant TG-AST080026N). This work was carried out at the Black Hole Initiative at Harvard University, which is supported by grants from the John Templeton Foundation and the Gordon and Betty Moore Foundation.

DATA AVAILABILITY

The data underlying this article will be shared on reasonable request to the corresponding author.

REFERENCES

Alexander K. D., Berger E., Guillochon J., Zauderer B. A., Williams P. K. G., 2016, ApJ, 819, L25
Alexander K. D., van Velzen S., Horesh A., Zauderer B. A., 2020, Space Sci. Rev., 216, 81
Andalman Z. L., Liska M. T. P., Tchekhovskoy A., Coughlin E. R., Stone N., 2022, MNRAS, 510, 1627
Anderson M. M. et al., 2020, ApJ, 903, 116
Andreoni I. et al., 2022, Nature, 612, 430
Baganoff F. K. et al., 2003, ApJ, 591, 891
Balbus S. A., Hawley J. F., 1991, ApJ, 376, 214
Barniol Duran R., Tchekhovskoy A., Giannios D., 2017, MNRAS, 469, 4957
Blandford R. D., Znajek R. L., 1977, MNRAS, 179, 433
Bloom J. S. et al., 2011, Science, 333, 203
Bondi H., 1952, MNRAS, 112, 195
Bonnerot C., Lu W., 2020, MNRAS, 495, 1374
Bonnerot C., Rossi E. M., Lodato G., Price D. J., 2016, MNRAS, 455, 2253
Bonnerot C., Lu W., Hopkins P. F., 2021, MNRAS, 504, 4885
Bricman K., Gomboc A., 2020, ApJ, 890, 73
Bromberg O., Tchekhovskoy A., 2016, MNRAS, 456, 1739
Burrows D. N. et al., 2011, Nature, 476, 421
Bustamante S., Springel V., 2019, MNRAS, 490, 4133
Chael A., Bouman K., Johnson M., Blackburn L., Shiokawa H., 2018, Eht-Imaging: Tools For Imaging And Simulating Vlbi Data, Zenodo
Chael A., Narayan R., Johnson M. D., 2019, MNRAS, 486, 2873
Chatterjee K., Liska M., Tchekhovskoy A., Markoff S. B., 2019, MNRAS, 490, 2200
Coughlin E. R., Begelman M. C., 2020, MNRAS, 499, 3158
Coughlin E. R., Quataert E., Ro S., 2018, ApJ, 863, 158
Curd B., 2021, MNRAS, 507, 3207
Curd B., Narayan R., 2019, MNRAS, 483, 565
Dai L., McKinney J. C., Roth N., Ramirez-Ruiz E., Miller M. C., 2018, ApJ, 859, L20
Doeleman S. et al., 2019, Bull. Am. Astron. Soc., 51, 256
Dotti M., Colpi M., Pallini S., Perego A., Volonteri M., 2013, ApJ, 762, 68
Dubois Y., Volonteri M., Silk J., 2014, MNRAS, 440, 1590
Eftekhari T., Berger E., Zauderer B. A., Margutti R., Alexander K. D., 2018, ApJ, 854, 86
Evans C. R., Kochanek C. S., 1989, ApJ, 346, L13
Event Horizon Telescope Collaboration, 2019, ApJ, 875, L3
Gammie C. F., McKinney J. C., Tóth G., 2003, ApJ, 589, 444
Gezari S., 2021, ARA&A, 59, 21
Gillessen S. et al., 2019, ApJ, 871, 126
Golightly E. C. A., Nixon C. J., Coughlin E. R., 2019, ApJ, 882, L26
Guillochon J., Ramirez-Ruiz E., 2013, ApJ, 767, 25
Guillochon J., Manukian H., Ramirez-Ruiz E., 2014, ApJ, 783, 23
Hawley J. F., Guan X., Krolik J. H., 2011, ApJ, 738, 84
Hayasaki K., Stone N., Loeb A., 2016, MNRAS, 461, 3760
Hervet O., Meliani Z., Zech A., Boisson C., Cayatte V., Sauty C., Sol H., 2017, A&A, 606, A103
Hills J. G., 1975, Nature, 254, 295
Howes G. G., 2010, MNRAS, 409, L104
Ivezić Ž. et al., 2019, ApJ, 873, 111
Kato Y., Mineshige S., Shibata K., 2004, ApJ, 605, 307
Kohler S., Begelman M. C., Beckwith K., 2012, MNRAS, 422, 2282
Komossa S., 2015, J. High Energy Astrophys., 7, 148
Lazzati D., Morsony B. J., Blackwell C. H., Begelman M. C., 2012, ApJ, 750, 68
Leloudas G. et al., 2019, ApJ, 887, 218
Liptai D., Price D. J., Mandel I., Lodato G., 2019, preprint (arXiv:1910.10154)
Liska M. T. P., Musoke G., Tchekhovskoy A., Porth O., Beloborodov A. M., 2022, ApJ, 935, L1
Mahadevan R., Narayan R., Yi I., 1996, ApJ, 465, 327
Mainetti D., Lupi A., Campana S., Colpi M., Coughlin E. R., Guillochon J., Ramirez-Ruiz E., 2017, A&A, 600, A124
McConnell N. J., Ma C.-P., 2013, ApJ, 764, 184
McKinney J. C., Tchekhovskoy A., Sadowski A., Narayan R., 2014, MNRAS, 441, 3177
Mizuno Y., Gómez J. L., Nishikawa K.-I., Meli A., Hardee P. E., Rezzolla L., 2015, ApJ, 809, 38
Mościbrodzka M., Gammie C. F., 2018, MNRAS, 475, 43
Mościbrodzka M., Falcke H., Shiokawa H., 2016, A&A, 586, A38
Narayan R., Igumenshchev I. V., Abramowicz M. A., 2003, PASJ, 55, L69
Narayan R., Chael A., Chatterjee K., Ricarte A., Curd B., 2022, MNRAS, 511, 3795
Novikov I. D., Thorne K. S., 1973, in DeWitt C., DeWitt B., eds, Black Holes (Les Astres Occlus). Gordon and Breach, London, p. 343
Ohmura T., Machida M., Nakamura K., Kudoh Y., Asahina Y., Matsumoto R., 2019, Galaxies, 7, 14
Ohmura T., Machida M., Nakamura K., Kudoh Y., Matsumoto R., 2020, MNRAS, 493, 5761

Table A1. Here, we indicate the resolution and grid type of each rerun of model `m10a0.9-HR`. Each rerun was evolved until $t = 25\,000\,t_g$. Note that the grid with added resolution only in the disc has the same grid settings, as in Curd & Narayan (2019), while the other models have the same grid setup, as in this paper (as described in Section 3.3).

Model name	Abbreviation	Resolution $N_r \times N_\vartheta$	Added resolution
`m10a0.9-LRa`	`LRa`	512 × 320	disc
`m10a0.9-LRb`	`LRb`	512 × 640	disc
`m10a0.9-IR`	`IR`	320 × 128	disc + jet
`m10a0.9-HR`	`HR`	640 × 256	disc + jet

Pasham D. R., van Velzen S., 2018, ApJ, 856, 1
Pasham D. R. et al., 2022, Nature Astron., in press
Penna R. F., Narayan R., Sądowski A., 2013, MNRAS, 436, 3741
Pfister H., Volonteri M., Dai J. L., Colpi M., 2020, MNRAS, 497, 2276
Pfister H., Dai J. L., Volonteri M., Auchettl K., Trebitsch M., Ramirez-Ruiz E., 2021, MNRAS, 500, 3944
Phinney E. S., 1989, in Morris M., ed., Proc. IAU Symp. 136, The Center of the Galaxy. Kluwer, Dordrecht, p.543
Ramirez-Ruiz E., Rosswog S., 2009, ApJ, 697, L77
Rees M. J., 1988, Nature, 333, 523
Ressler S. M., Tchekhovskoy A., Quataert E., Gammie C. F., 2017, MNRAS, 467, 3604
Reynolds C. S., 2013, Class. Quantum Gravity, 30, 244004
Rowan M. E., Sironi L., Narayan R., 2017, ApJ, 850, 29
Rybicki G. B., Lightman A. P., 1979, Radiative Processes in Astrophysics. Wiley, New York
Schechter P., 1976, ApJ, 203, 297
Shiokawa H., Krolik J. H., Cheng R. M., Piran T., Noble S. C., 2015, ApJ, 804, 85
Sądowski A., Narayan R., 2015a, MNRAS, 453, 3213
Sądowski A., Narayan R., 2015b, MNRAS, 454, 2372
Sądowski A., Narayan R., Tchekhovskoy A., Zhu Y., 2013, MNRAS, 429, 3533
Sądowski A., Narayan R., McKinney J. C., Tchekhovskoy A., 2014, MNRAS, 439, 503
Sądowski A., Narayan R., Tchekhovskoy A., Abarca D., Zhu Y., McKinney J. C., 2015, MNRAS, 447, 49
Sądowski A., Wielgus M., Narayan R., Abarca D., McKinney J. C., Chael A., 2017, MNRAS, 466, 705
Stein R. et al., 2021, Nature Astron., 5, 510
Steinberg E., Stone N. C., 2022, preprint (arXiv:2206.10641)
Stone N. C., Metzger B. D., 2016, MNRAS, 455, 859
Stone N., Sari R., Loeb A., 2013, MNRAS, 435, 1809
Sun H., Zhang B., Li Z., 2015, ApJ, 812, 33
Sutherland R. S., Dopita M. A., 1993, ApJS, 88, 253
Tchekhovskoy A., Narayan R., McKinney J. C., 2011, MNRAS, 418, L79
Tchekhovskoy A., McKinney J. C., Narayan R., 2012, J. Phys.: Conf. Ser., 372, 012040
Tchekhovskoy A., Metzger B. D., Giannios D., Kelley L. Z., 2014, MNRAS, 437, 2744
van Velzen S. et al., 2021, ApJ, 908, 4
Wevers T. et al., 2022, A&A, 666, A6

APPENDIX A: EFFECTS OF JET RESOLUTION ON DYNAMICS

To test the impact of the chosen grid resolution on the jet dynamics, we conducted a suite of reruns using the same initial conditions as model `m10a0.9-HR` but for various grid resolutions. We describe each simulation in Table A1 and compare the resulting jet at the same simulation time in Fig. A1. Each rerun was run to $t = 25\,000\,t_g$, which is ample time for the accretion flow to evolve and produce a jet. Note that we use abbreviated names for the models for simplicity in the following paragraphs.

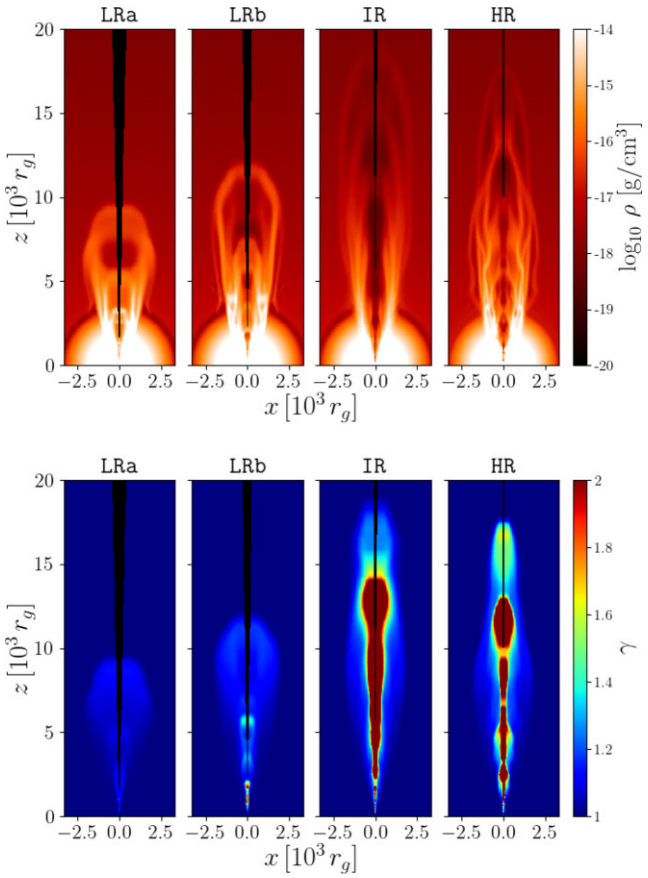

Figure A1. Here, we show the gas density (top panels) and lorentz factor (bottom panels) at $t = 25\,000\,t_g$ for each model in Table A1. Note that the abbreviated model name is given above each panel. The resolution within the jet increases from left to right. As the resolution increases, we generally find that the acceleration of gas near the pole is better captured. Of note is the need for cylindrification and high resolution near the pole to capture both the acceleration and recollimation shocks properly, as can be seen by comparing `IR` and `HR`.

Model `LRa` employs the same grid resolution as Curd & Narayan (2019), which had an increased resolution around $\vartheta = \pi/2$, but sacrificed resolution in the jet (giving a five times smaller angular resolution near the pole compared to model `HR`). The angular coordinate ϑ is related to a code coordinate x_2. The precise relationship is given by

$$\vartheta = \frac{\pi}{2}\left[1 + \cot\left(\frac{\pi}{2}H_0\right)\tan\left(H_0\pi(x_2 - \frac{1}{2})\right)\right], \tag{A1}$$

where H_0 is a parameter, which increases the resolution around $\vartheta = \pi/2$ as it approaches unity. For Curd & Narayan (2019) and the simulations in this appendix, we choose $H_0 = 0.7$. As with the simulations presented in the main text, we copy the primitives from the third cell from the polar axis to bolster numerical stability. The jet in `LRa` evolves in a similar way as `s09` in Curd & Narayan (2019). The maximum γ is less than 2, indicating the resolution is too poor to capture the evolution of the jet near the polar axis. When the angular resolution is doubled in `LRb`, we begin to see greater acceleration of the jet but only marginally so.

For models `IR` and `HR`, we employ the same grid choices as described in Section 3.3 but with differing resolution choices. Model

IR employs an identical grid to HR but with half the resolution in both r and ϑ. Although the total number of cells in both r and ϑ is lower, the added resolution and the cylindrification of the grid near the polar axis allows us to capture the acceleration of relativistic material. However, comparing IR to HR, we find that yet higher resolution is necessary to capture recollimation shocks, which contribute to the structure and evolution of the jet.

We must point out that the jets in these models impact the radio-submillimetre emission. However, the higher energy emission (optical to X-ray) is dominated by the torus and inner accretion disc since comptonization in the jet is weak. Hence, the qualitative viewing angle effects in optical/UV/X-ray spectra reported in Curd & Narayan (2019) for s09 will be unchanged by resolving the jet properly.

APPENDIX B: ADDITIONAL FIGURES

Here, we show additional figures for comparison with fiducial models described in the text. We show the jet properties of m5a0.5-HR in Fig. B1. Compared to m5a0.0-HR, the jet has travelled nearly the same distance ($\sim 40\,000\,r_{\rm g}$), but the jet core is much faster and the gas temperature in the core is hotter. In addition, the magnetic field strength along the jet axis is larger.

We show the jet properties of m10a0.9-HR in Fig. B2. Compared to m5a0.9-HR, the jet features are generally similar. This is in well agreement with the general result that we find throughout this work that the BH mass does not have a noticeable effect on the jet. The most important factor is instead the BH spin.

In Fig. B3, we show the 230 GHz jet emission viewed at 90° near its brightest point in each simulation.

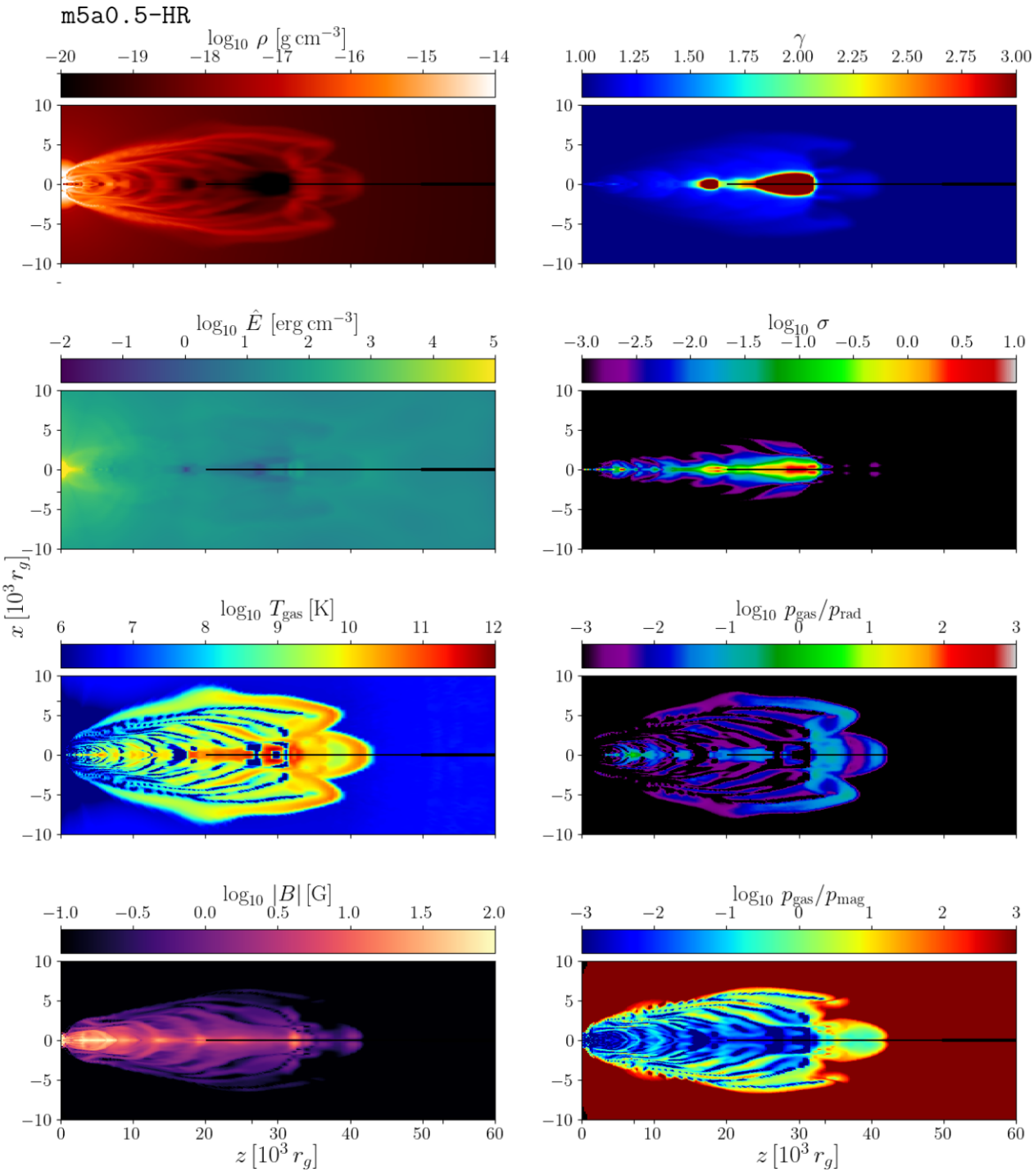

Figure B1. The same as Fig. 8 but for `m5a0.5-HR`.

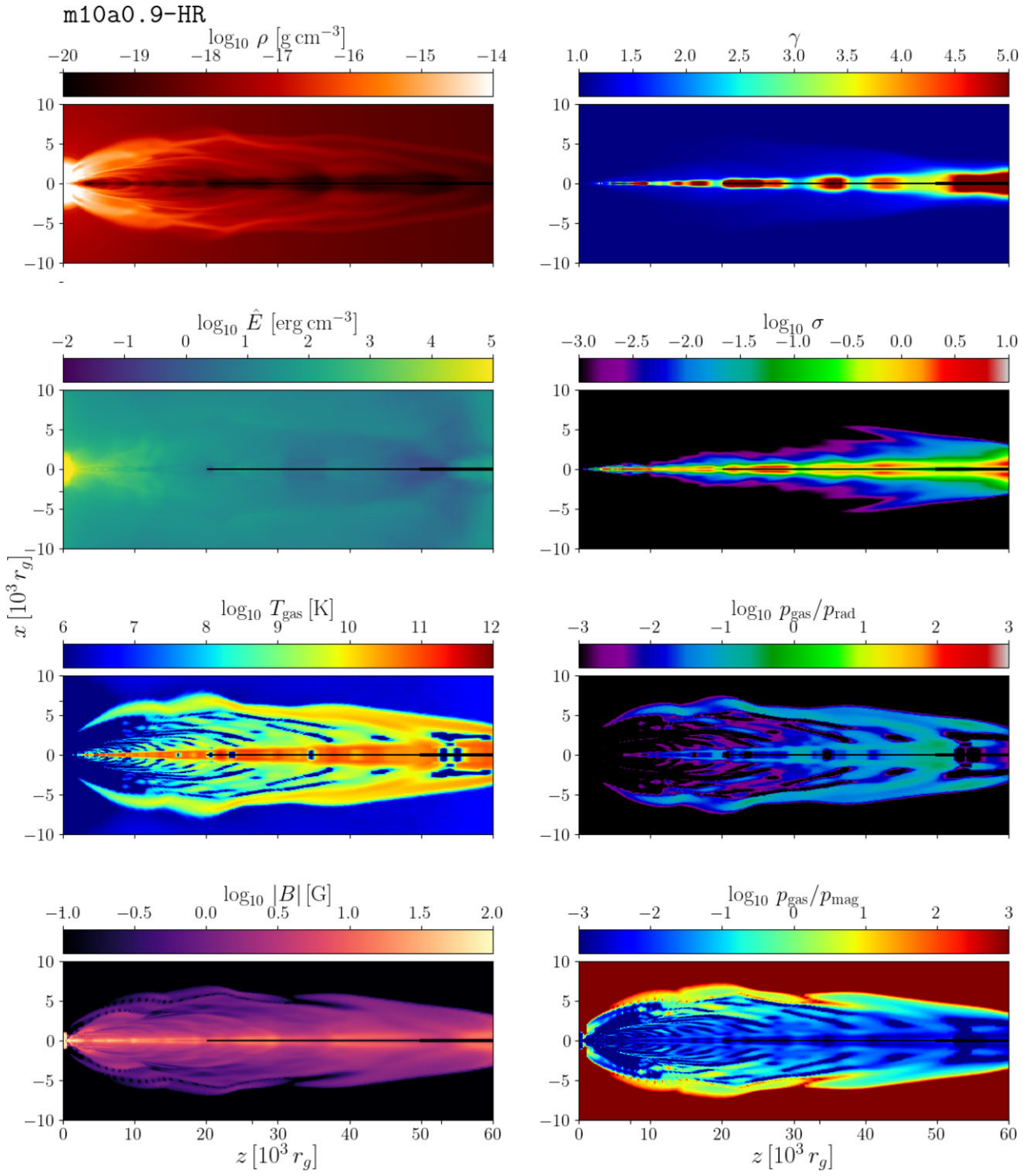

Figure B2. The same as Fig. 8 but for `m10a0.9-HR`.

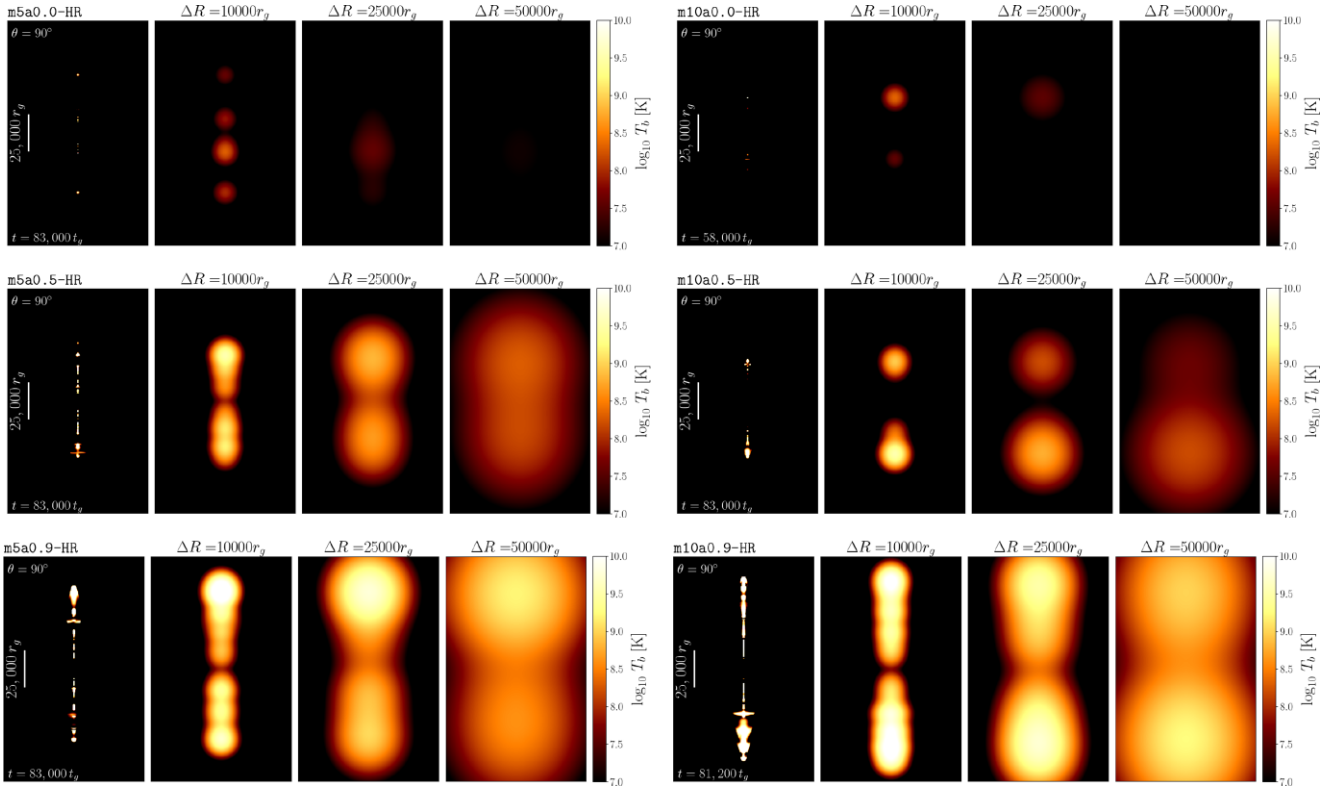

Figure B3. Here, we compare the jets for each model viewed at 90°. The simulation time ray traced in each image is $t = 83\,000\, t_g$ for models `m5a0.0-HR`, `m5a0.5-HR`, `m5a0.9-HR`, and `m10a0.5-HR`, $t = 58\,000\, t_g$ for model `m10a0.0-HR`, and $t = 81\,200\, t_g$ for model `m10a0.9-HR`. The time is also specified at the bottom-left of the left-most panel for each model.

This paper has been typeset from a TEX/LATEX file prepared by the author.